

Coulomb Correlations in 4d and 5d Oxides from First Principles - or How Spin-Orbit Materials choose their Effective Orbital Degeneracies

Cyril Martins¹, Markus Aichhorn², and Silke Biermann^{3,*}

¹*Laboratoire de Chimie et Physique Quantiques, UMR 5626, Université Paul Sabatier, 118 route de Narbonne, 31400 Toulouse, France*

²*Institute of Theoretical and Computational Physics, Technical University Graz, Petersgasse 16, Graz, Austria*

³*Centre de Physique Théorique, Ecole Polytechnique, CNRS UMR 7644, Université Paris-Saclay, 91128 Palaiseau, France*

Abstract

The interplay of spin-orbit interactions and Coulomb correlations has become a hot topic in condensed matter theory. Here, we review recent advances in dynamical mean-field theory-based electronic structure calculations for iridates and rhodates. We stress the notion of the *effective degeneracy* of the compounds, which introduces an additional axis into the conventional picture of a phase diagram based on filling and on the ratio of interactions to bandwidth.

1 Introduction

Electronic Coulomb correlations are at the heart of a variety of exotic properties in compounds with partially filled 3d or 4f shells. Prominent examples are found among the 3d transition metal oxides, where unconventional transport behaviors, ordering phenomena or unusual spectroscopic properties are observed [1]. It was argued early on that the comparably weak spatial extension of 3d orbitals leads to large electronic Coulomb interactions, competing with kinetic contributions. Depending on crystal fields, hybridisation, Hund's exchange, and band filling, this interplay can lead to renormalised metallic behavior such as in simple oxides like SrVO₃ [2, 3] or iron pnictide compounds [4–9] or induce Mott insulating behavior like in YTiO₃ [10] or V₂O₃ [11–14]. According to common belief until recently, such effects would be less dramatic in 4d and even less in 5d compounds, due to the substantially more extended radial wave functions of those shells, as shown in Fig. 1. The discovery of Mott insulating behavior in Sr₂IrO₄ therefore triggered a little revolution in the field [15, 16]. In 5d oxides, spin-orbit coupling acts

*silke.biermann@polytechnique.edu

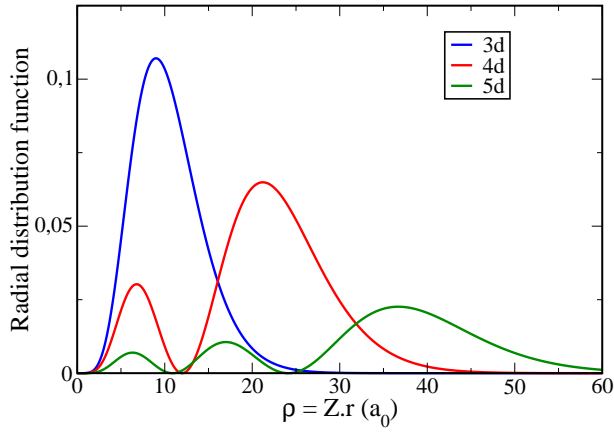


Figure 1: Radial distribution function $r^2 R_{n\ell}(r)^2$ as a function of the distance from the nucleus r expressed in atomic units, for the 3d, 4d and 5d orbitals. To ease the comparison between different atoms, we use the renormalized distance $\rho = Z.r$ on the abscissa, where Z is the effective nuclear charge for a given multi-electron atom. As the principal quantum number n increases, Z remains almost constant for d valence electrons and their radial distribution is thus more and more extended.

on an energy scale comparable to the other scales of the system (Coulomb interactions, bandwidths, ligand fields ...), and the electronic state is the result of a complex interplay of Coulomb correlations, spin-orbit splitting and crystal field effects (for recent reviews see [17, 18]). But, as pointed out already earlier [19, 20], also in 4d compounds spin-orbit interactions can influence the electronic properties substantially. In Sr_2RhO_4 , for example, the experimentally observed Fermi surface can only be reconciled with experiments when spin-orbit coupling and electronic Coulomb correlations are taken into account [19–22]. Here, we give a review of recent efforts to describe correlated spin-orbit physics from first principles, in a combined density functional and dynamical mean-field theory framework [21].

2 Spin-orbit materials – an incomplete literature review

The term *spin-orbit material* refers to systems where spin-orbit coupling (SOC) and its interplay with other elements of the electronic structure – crystal or ligand fields, Coulomb correlations, magnetism, ... – is essential in determining the physical properties. In many such materials, the physics is largely determined by the geometrical aspects of the crystalline structure, and the electronic properties can be understood by analysing the one-particle band structure. In particular, strong enough spin-orbit coupling can cause band inversions, possibly leading to non-trivial topological effects. The quest for topological materials is nowadays a hot topic of condensed matter physics, and several excellent reviews exist in the literature [23–25].

The scope of the present review is however a different one. Here, we focus on materials, where the interplay of spin-orbit interactions and Coulomb correlations is crucial, and the band picture is at best useful as a starting point for further many-body calculations. Early examples are found among the layered tantalum chalcogenides: TaS_2 [26–28] is Mott insulating thanks to the presence of a lone narrow band resulting from the combined effect of SOC and a charge-density wave instability. The corresponding selenide, TaSe_2 [29] displays a surface Mott metal-insulator

transition. Nevertheless, the true power of the interplay of spin-orbit interactions was fully appreciated only after the discovery of Sr_2IrO_4 : the insulating behavior – despite of moderate Coulomb interactions usually present in 5d compounds – was even more intriguing, as the electronic and crystal structures are otherwise seemingly simple. The interplay of Coulomb correlations and spin-orbit coupling was indeed shown to be essential to drive the system insulating, leading to a state dubbed “spin-orbit Mott insulator” [15, 16]. A flurry of further spin-orbit materials have by now been characterized, or known compounds have been reinvestigated in the light of new insights. Iridium-based materials, where several families of compounds have been studied systematically, still hold a privileged position. Tab. 1 summarizes the structural, transport and magnetic properties of a selection of iridates. It is interesting to note that the large majority among them display insulating phases. The Ir^{4+} ($5d^5$) state does not allow for a band insulating state without symmetry breaking, and magnetic order is an obvious candidate for helping in opening the gap. Nevertheless, few compounds have been unambiguously characterized as Slater insulators.

Slightly more recently, attention focussed yet onto another class of 5d materials, namely osmium-based compounds. In this class fall for example ferroelectric LiOsO_3 [30] as well as the prototypical Slater insulator NaOsO_3 [31–36] where the loss of magnetic order with increasing temperature is accompanied by a closure of the insulating gap. It has been realised, however, that SOC can also have notable effects in 4d compounds, with prominent examples among ruthenium- and rhodium-based materials, where most interesting consequences for magnetic excitations have been discussed [37]. Tab. 2 gives an overview of the properties of a selection of osmates, ruthenates and rhodates. In the following discussion, we will restrict ourselves to the prototypical correlated iridate Sr_2IrO_4 and its 4d analog, Sr_2RhO_4 .

2.1 Correlated spin-orbit insulators: the example of Sr_2IrO_4

The 5d transition metal oxide (TMO) Sr_2IrO_4 has a tetragonal crystal structure, the symmetry of which is lowered from the K_2NiF_4 -type, well-known in Sr_2RuO_4 or La_2CuO_4 , by an 11° rotation of its IrO_6 octahedra around the c -axis [136]. Each Ir atom accomodates 5 electrons and the standard picture neglecting spin-orbit interactions would give a “ t_{2g}^5 ” ground state. However, this compound exhibits insulating behavior up to the highest measured temperatures, with a strongly temperature-dependent gap. The optical gap at room temperature is about 0.26 eV [137]. Below $T_N = 240$ K, a canted-antiferromagnetic (AF) order sets in, with an effective local moment of $0.5 \mu_B/\text{Ir}$, and a saturation moment of $0.14 \mu_B/\text{Ir}$ [138]. This phase has triggered much experimental and theoretical work [139–142], highlighting in particular the importance of the SOC.

Here, we focus on the paramagnetic phase, above 240 K, which is most interesting due to the persistence of the insulating nature despite the absence of magnetic order, as shown by transport measurements [15], by scanning tunneling microscopy and spectroscopy experiments [143], by angle-resolved spectroscopy [16, 144], time-resolved spectroscopy [145, 146] or optical conductivity [137].

Resonant Inelastic X-ray spectroscopy (RIXS) experiments [15] have early on proposed a picture in terms of $j_{\text{eff}}=1/2$ and $j_{\text{eff}}=3/2$ states:

Iridium-based spin-orbit materials							
Compound	Crystal Struct.		Transport Property		Magnetic Ordering		Ref.
CaIrO ₃	post-perovskite	<i>Cmcm</i>	Ins.	gap: 0.34 eV	AFM	$T_N = 115$ K	[38–40]
NaIrO ₃	post-perovskite	<i>Cmcm</i>	Ins.	–	None		[41, 42]
BaIrO ₃	monoclinic	<i>C2/m</i>	Ins.	gap: 0.05 eV	FM	$T_C = 180$ K	[43–45]
SrIrO ₃	monoclinic	<i>C2/c</i>	Metal		None		[46–49]
α -Na ₂ IrO ₃	honeycomb monoclinic	<i>C2/c</i>	Ins.	gap: 0.35 eV	zig-zag AFM	$T_N = 15$ K	[50–55]
α -Li ₂ IrO ₃	honeycomb monoclinic	<i>C2/c</i>	Ins.	–	spiral AFM	$T_N = 15$ K	[56, 57]
β -Li ₂ IrO ₃	hyperhoneycomb	<i>Fddd</i>	Ins.	–	unconventional AFM	$T_N = 38$ K	[58, 59]
γ -Li ₂ IrO ₃	stripyhoneycomb	<i>Cccm</i>	Ins.	–	unconventional AFM	$T_N = 38$ K	[60]
Ba ₂ IrO ₄	K ₂ NiF ₄ -type	<i>I4/mmm</i>	Ins.	gap: 0.14 eV	AFM	$T_N = 240$ K	[61–64]
Sr ₂ IrO ₄	distorted K ₂ NiF ₄ -type	<i>I4₁/acd</i>	Ins.	gap 0.25 eV	canted AFM	$T_N = 240$ K	[15, 16, 21]
Ca ₄ IrO ₆	hexagonal	<i>R3c</i>	Ins.	–	AFM	$T_N = 13.95$ K	[65–67]
Y ₂ Ir ₂ O ₇	pyrochlore	<i>Fd3m</i>	Ins.	–	AIAO	$T = 155$ K	[68, 69]
Pr ₂ Ir ₂ O ₇	pyrochlore	<i>Fd3m</i>	Metal		None		[70, 71]
Nd ₂ Ir ₂ O ₇	pyrochlore	<i>Fd3m</i>	MIT	$T = 36$ K	AIAO	$T = 36$ K	[70, 72]
Sm ₂ Ir ₂ O ₇	pyrochlore	<i>Fd3m</i>	MIT	$T = 117$ K	AIAO	$T = 117$ K	[70, 72]
Eu ₂ Ir ₂ O ₇	pyrochlore	<i>Fd3m</i>	MIT	$T = 120$ K	AIAO	$T = 120$ K	[70, 73–75]
Gd ₂ Ir ₂ O ₇	pyrochlore	<i>Fd3m</i>	Ins.	–	AIAO	$T = 127$ K	[70]
Tb ₂ Ir ₂ O ₇	pyrochlore	<i>Fd3m</i>	Ins.	–	AIAO	$T = 130$ K	[70, 76]
Dy ₂ Ir ₂ O ₇	pyrochlore	<i>Fd3m</i>	Ins.	–	AIAO	$T = 134$ K	[70]
Ho ₂ Ir ₂ O ₇	pyrochlore	<i>Fd3m</i>	Ins.	–	AIAO	$T = 141$ K	[70]
Er ₂ Ir ₂ O ₇	pyrochlore	<i>Fd3m</i>	Ins.	–	AIAO	$T = 140$ K	[76]
Yb ₂ Ir ₂ O ₇	pyrochlore	<i>Fd3m</i>	Ins.	–	AIAO	$T = 130$ K	[77]
Lu ₂ Ir ₂ O ₇	pyrochlore	<i>Fd3m</i>	Ins.	–	AIAO	$T = 120$ K	[78]
Bi ₂ Ir ₂ O ₇	pyrochlore	<i>Fd3m</i>	Metal		None		[79, 80]
Sr ₃ Ir ₂ O ₇	monoclinic	<i>C2/c</i>	Ins.	gap: 0.1 eV	AFM	$T_N = 285$ K	[46, 81–85]
Na ₄ Ir ₃ O ₈	hyperkagome	<i>P4₁32</i>	Ins.	–	AFM	$T_N = 6$ K	[86–88]
Ca ₅ Ir ₃ O ₁₂	hexagonal	<i>P – 62m</i>	Ins.	–	AFM	$T_N = 7.8$ K	[66, 67, 89]
La ₂ ZnIrO ₆	double-perovskite	<i>P2₁/n</i>	Ins.	–	FM	$T_C = 7.5$ K	[90]
La ₂ MgIrO ₆	double-perovskite	<i>P2₁/n</i>	Ins.	gap: 0.16 eV	AFM	$T_N = 12$ K	[90, 91]
Pr ₂ MgIrO ₆	double-perovskite	<i>P2₁/n</i>	Ins.	gap: 0.2 eV	AFM	$T_N = 14$ K	[91, 92]
Nd ₂ MgIrO ₆	double-perovskite	<i>P2₁/n</i>	Ins.	–	AFM	$T_N = 12$ K	[92]
Sm ₂ MgIrO ₆	double-perovskite	<i>P2₁/n</i>	Ins.	–	AFM	$T_N = 15$ K	[92]
Eu ₂ MgIrO ₆	double-perovskite	<i>P2₁/n</i>	Ins.	–	AFM	$T_N = 10$ K	[92]
Gd ₂ MgIrO ₆	double-perovskite	<i>P2₁/n</i>	Ins.	–	None		[92]
Sr ₂ CeIrO ₆	double perovskite	<i>P2₁/n</i>	Ins.	gap: 0.3 eV	AFM	$T_N = 21$ K	[93–95]
Ba ₂ YIrO ₆	double perovskite	<i>Fm3m</i>	Ins.	gap: 0.221 eV	None		[96]
Ba ₃ IrTi ₂ O ₉	hexagonal	<i>P6₃mc</i>	Ins.	–	None		[97, 98]
Ba ₃ ScIr ₂ O ₉	hexagonal	<i>P6₃/mmc</i>	Ins.	–	None		[99]
Ba ₃ YIr ₂ O ₉	hexagonal	<i>P6₃/mmc</i>	Ins.	–	FM	$T = 4$ K	[99]
Ba ₃ ZnIr ₂ O ₉	hexagonal	<i>P6₃/mmc</i>	Ins.	–	None		[100]

Table 1: Main structural, transport and magnetic properties of Ir-based spin-orbit materials. In the third column, Ins. refers to *insulator* and MIT to *metal-insulator transition*. The notations AFM, FM and AIAO refer to a *antiferromagnetic*, *ferromagnetic* and *all-in-all-out* magnetic ordering respectively.

$$\begin{aligned}
\left| j_{\text{eff}} = \frac{1}{2}, m_{j_{\text{eff}}} = +\frac{1}{2} \right\rangle &= +\frac{1}{\sqrt{3}} \left(|d_{yz}, \downarrow\rangle + i |d_{xz}, \downarrow\rangle \right) + \frac{1}{\sqrt{3}} |d_{xy}, \uparrow\rangle \\
\left| j_{\text{eff}} = \frac{1}{2}, m_{j_{\text{eff}}} = -\frac{1}{2} \right\rangle &= +\frac{1}{\sqrt{3}} \left(|d_{yz}, \uparrow\rangle - i |d_{xz}, \uparrow\rangle \right) - \frac{1}{\sqrt{3}} |d_{xy}, \downarrow\rangle
\end{aligned} \tag{1}$$

$$\begin{aligned}
\left| j_{\text{eff}} = \frac{3}{2}, m_{j_{\text{eff}}} = +\frac{1}{2} \right\rangle &= -\frac{1}{\sqrt{6}} \left(|d_{yz}, \downarrow\rangle + i |d_{xz}, \downarrow\rangle \right) + \sqrt{\frac{2}{3}} |d_{xy}, \uparrow\rangle \\
\left| j_{\text{eff}} = \frac{3}{2}, m_{j_{\text{eff}}} = -\frac{1}{2} \right\rangle &= +\frac{1}{\sqrt{6}} \left(|d_{yz}, \uparrow\rangle - i |d_{xz}, \uparrow\rangle \right) + \sqrt{\frac{2}{3}} |d_{xy}, \downarrow\rangle \\
\left| j_{\text{eff}} = \frac{3}{2}, m_{j_{\text{eff}}} = +\frac{3}{2} \right\rangle &= -\frac{1}{\sqrt{2}} \left(|d_{yz}, \uparrow\rangle + i |d_{xz}, \uparrow\rangle \right) \\
\left| j_{\text{eff}} = \frac{3}{2}, m_{j_{\text{eff}}} = -\frac{3}{2} \right\rangle &= +\frac{1}{\sqrt{2}} \left(|d_{yz}, \downarrow\rangle - i |d_{xz}, \downarrow\rangle \right)
\end{aligned} \tag{2}$$

Since the quartet of states lies lower in energy than the doublet and the splitting between the $j_{\text{eff}}=3/2$ and $j_{\text{eff}}=1/2$ is large, neglecting any band dispersion would result in a configuration

Compound	Crystal Struct.	Transport Property	Magnetic Ordering	Ref.
Ruthenium-based spin-orbit materials				
BaRuO ₃	cubic perovskite	$Pm\bar{3}m$	Metal	FM $T_c = 60$ K [101–103]
CaRuO ₃	perovskite	$Pnma$	Metal	None [104–106]
SrRuO ₃	perovskite	$Pnma$	Metal	FM $T_c = 160$ K [104, 106, 107]
Sr ₂ RuO ₄	K ₂ NiF ₄ -type	$I4/mmm$	Metal	None [108, 109]
Ca ₂ RuO ₄	distorted K ₂ NiF ₄ -type	$Pbca$ or $P2_1/c$	MIT $T = 357$ K	AFM $T = 110$ K [108, 110–112]
Sr ₂ RuO ₆	hexagonal	$P\bar{3}1m$	Ins. –	AFM $T_N = 565$ K [113, 114]
Sr ₃ Ru ₂ O ₇	orthorhombic	$BBcb$	Metal	None [106, 115]
Sr ₄ Ru ₃ O ₁₀	orthorhombic	$Pbam$	Metal	FM $T_c = 105$ K [106, 116, 117]
Rhodium-based spin-orbit materials				
Li ₂ RhO ₃	honeycomb	$C2/m$	Ins. gap: 0.08 eV	None [118, 119]
Sr ₂ RhO ₄	distorted K ₂ NiF ₄ -type	$I4_1acd$	Metal	None [21, 120, 121]
Sr ₄ RhO ₆	hexagonal	$R\bar{3}c$	Ins. gap: 0.1 eV	AFM $T_N = -$ K [122]
Sr ₅ Rh ₄ O ₁₂		$P3c1$	Ins. –	AFM $T_N = 23$ K [66, 123]
Osmium-based spin-orbit materials				
BaOsO ₃	six-layer hexagonal 6H	$Pm\bar{3}m$	Metal	None [124, 125]
CaOsO ₃	perovskite	$Pnma$	Metal	None [125]
SrOsO ₃	perovskite	$Pnma$	Metal	None [125]
NaOsO ₃	perovskite	$Pnma$	MIT $T = 410$ K	AFM $T = 410$ K [31–36]
Cd ₂ Os ₂ O ₇	pyrochlore	$Fd\bar{3}m$	MIT $T = 226$ K	AIAO $T = 226$ K [126–129]
Ba ₂ NaOsO ₆	double-perovskite	$Fm\bar{3}m$	Ins. –	FM $T_c = 6.8$ K [130–132]
Ba ₂ LiOsO ₆	double-perovskite	$Fm\bar{3}m$	Ins. –	AFM $T_N = 8$ K [131]
Ba ₂ CaOsO ₆	double-perovskite	$Fm\bar{3}m$	Ins. –	FM $T_c = 50$ K [133, 134]
Ba ₂ YO ₆	double-perovskite	$Fm\bar{3}m$	Ins. –	AFM $T_N = 69$ K [134, 135]

Table 2: Main structural, transport and magnetic properties of Ru,Rh and Os-based spin-orbit materials. In the third column, Ins. refers to *insulator* and MIT to *metal-insulator transition*. The notations AFM, FM and AIAO refer to a *antiferromagnetic*, *ferromagnetic* and *all-in-all-out* magnetic ordering respectively.

with one electron in the $j_{\text{eff}}=1/2$ state. The DFT band structure displays a dispersion of width comparable to this splitting, leaving the question *a priori* open again. However, the bandwidth is narrowed due to structural distortions [21], and electronic correlations can then become effective and eventually drive the compound insulating.

Since the discovery of this mechanism, other Ir-based compounds (cf. Tab. 1) have been classified as spin-orbit Mott insulators (Na₂IrO₃, pyrochlores, etc...). Recent theoretical studies predict also some fluoride material [147] to be in this class. The one-orbital nature of insulating Sr₂IrO₄ has contributed to intense activities attempting to dope the compound, with the hope of inducing a superconducting state as in the cuprates. Doping-induced metal-insulator transitions and the properties of the metallic phases have therefore become a hot topic, with studies of various compounds, e.g. Sr₂IrO₄ [144, 148], (Sr_{1-x}La_x)₃Ir₂O₇ [149], Ca_{1-x}Sr_xIrO₃ [150], Ca_{1-x}Ru_xIrO₃ [151], Sr₂Ir_{1-x}Rh_xO₄ [152, 153], Sr₂Ir_{1-x}Ru_xO₄ [154], Sr_xLa_{11-x}Ir₄O₂₄ [155].

2.2 Correlated spin-orbit metals: the example of Sr₂RhO₄

It is natural that also in *metallic* 4d or 5d transition metal compounds, SOC can have notable consequences. An example of a “spin-orbit correlated metal” is the end member SrIrO₃ of the Ir-based Ruddlesden-Popper Sr_{n+1}Ir_nO_{3n+1} series [46] but also many Ru-,Rh- or Os-based transition metal oxides (TMOs) belong to this class (cf. Tab. 1 and 2). In these compounds, correlations are important enough to renormalize the Fermi surface – albeit in a strongly spin-orbit coupling-dependent way. The respective roles of both effects have been worked out in some details for several compounds, among which SrIrO₃ [46–48], Sr₂RuO₄/Ca₂RuO₄ [108, 109, 156]

and Sr_2RhO_4 [19–21].

We will focus our attention in the following on Sr_2RhO_4 motivated by its structural proximity and isoelectronic nature to Sr_2IrO_4 . Indeed, this TMO is the 4d counterpart of Sr_2IrO_4 , both concerning structure and filling. Understanding its Fermi surface requires to include both SOC and correlations [21]. It is composed of three pockets (cf. Fig. 8): a circular hole-like α -pocket around Γ , a lens-shaped electron pocket β_M and a square-shaped electron pocket β_X with a mass enhancement of 3.0, 2.6 and 2.2 respectively [120].

In this review, we will put Sr_2IrO_4 and Sr_2RhO_4 in parallel, shedding light on the spectral properties of these compounds and elaborating on the notion of a reduced effective (spin-orbital) degeneracy that is crucial for their properties.

2.3 Spin-orbit coupling and cubic symmetry: the j_{eff} picture

Necessary conditions for realising a j_{eff} picture are (1) a strong spin-orbit coupling constant and (2) an important cubic crystal field. These conditions are often met in crystalline structures where IrO_6 octahedra are present (cf. Tab. 1). Similar compounds based on Ru, Rh and Os also show such j_{eff} states (cf. Tab 2). However, not all Ir-based structures belong to this case : we note that neither epitaxial thin films of IrO_2 [157] nor the correlated metal IrO_2 in its rutile structure [158, 159] exhibit such $j_{\text{eff}}=1/2$ state. We will now turn to a more precise description of that picture.

The spin-orbit interaction is one of the relativistic corrections to the Schrödinger-Pauli equation arising when taking the non-relativistic limit of Dirac’s equation. It introduces a coupling between the spin \mathbf{S} and the motion – or more precisely the orbital momentum \mathbf{L} in the atomic case – of the electron. In a solid described within an independent-particle picture, spin-orbit coupling has the following general form:

$$H_{SO} = \frac{\hbar}{4m_0^2c^2} \boldsymbol{\sigma} \cdot [\nabla V(\mathbf{r}) \times \mathbf{p}] \quad (3)$$

where m_0 is the electron mass, $V(\mathbf{r})$ is the effective Kohn-Sham potential and $\sigma_{i=x,y,z}$ denote the Pauli-spin matrices. Assuming that the potential close to the nucleus has spherical symmetry the mean value of the spin-orbit interaction on the atomic state (n, ℓ) takes the more common form:

$$H_{SO} = \zeta_{SO}(n\ell) \mathbf{l} \cdot \mathbf{s} \quad \text{with} \quad \zeta_{SO}(n\ell) = \frac{\hbar^2}{2m_0^2c^2} \left\langle \frac{1}{r} \frac{dV}{dr} \right\rangle_{(n,\ell)} \quad (4)$$

where $\mathbf{S} = \frac{1}{2}\boldsymbol{\sigma}$, $\mathbf{L} = \mathbf{r} \times \mathbf{p} = \hbar \mathbf{l}$ and $\langle \dots \rangle_{(n,\ell)}$ denotes the mean value of the radial quantity in the state (n, ℓ) . Tab. 3 gives some values of the spin-orbit constant ζ_{SO} for 3d, 4d and 5d atoms. The SOC increases with the atomic number, explaining why spin-orbit materials are mostly found in 5d and 4d TMOs.

Due to the effect of SOC, a multiplet splitting arises in the d -orbitals. Fig. 2 shows the multiplet splitting of d -orbitals due to the spin-orbit coupling as a function of the strength of a cubic crystal field $\Delta = 10Dq$.

In spherical symmetry the fine structure is composed of a six-fold $J = 5/2$ multiplet (in red) and a $J = 3/2$ quartet of lower energy (in blue), following "Landé’s interval rule". The presence

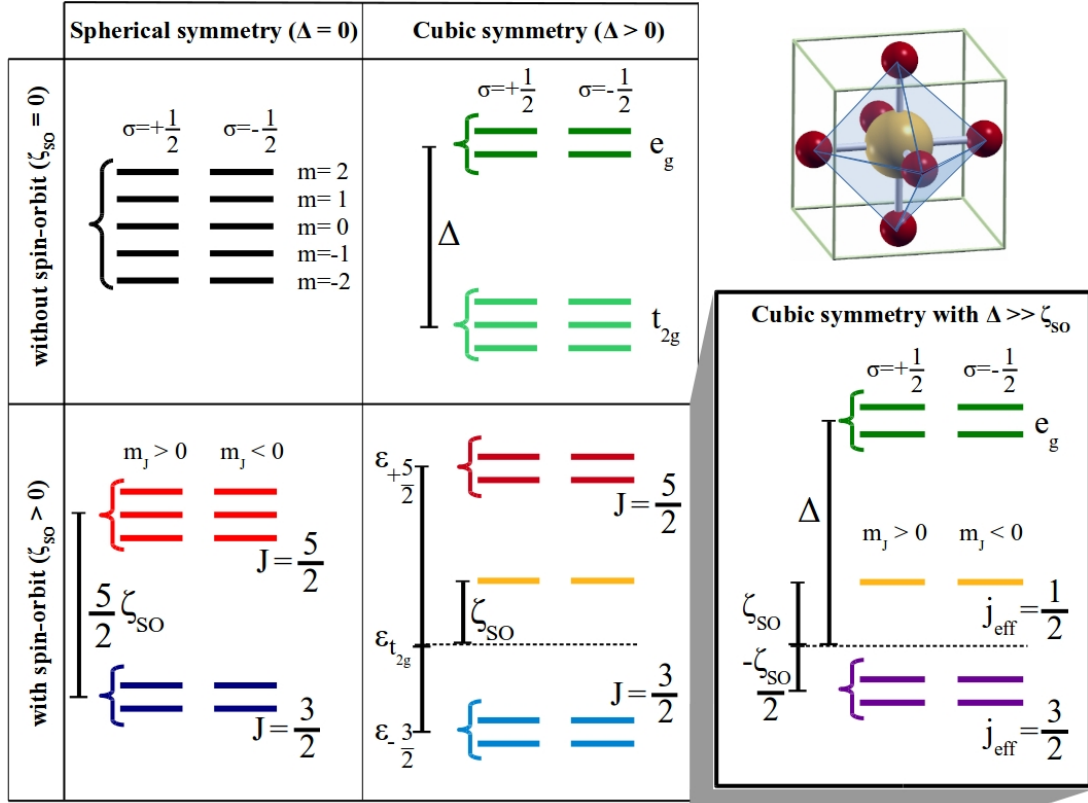


Figure 2: Orbital diagrams for the d -shell of an atom as a function of a cubic crystal field Δ and spin-orbit coupling ζ_{so} , paramagnetic case. Starting from the d -shell in spherical symmetry, the cubic crystal field splits them into e_g and t_{2g} , while the SOC creates a 6-fold $J = 5/2$ multiplet and a $J = 3/2$ quartet of lower energy. When both parameters are at stake, one gets a new multiplet structure where J remains a good quantum number but not J_z . The initial $J = 5/2$ multiplet splits into a quartet and a doublet of lower energy, while the quartet $J = 3/2$ undergoes some redefinition inside its submanifold. The energetic splitting and the nature of the spin-orbitals depend on the ratio between Δ/ζ_{so} . An exception is the doublet which is already of the form of the $j_{eff}=1/2$. In the limit where $\Delta \gg \zeta_{so}$, as is the case in the compounds of our interest, one gets the celebrated splitting into e_g , $j_{eff}=1/2$ and $j_{eff}=3/2$.

Atom	Z	$\zeta_{SO}(3d)$	Atom	Z	$\zeta_{SO}(4d)$	Atom	Z	$\zeta_{SO}(5d)$
Fe	26	0.050 eV	Ru	44	0.161 eV	Os	76	0.31 eV
Co	27	0.061 eV	Rh	45	0.191 eV	Ir	77	0.4 eV
Cu	29	0.103 eV	Ag	47	0.227 eV	Au	79	0.42 eV

Table 3: Value of the spin-orbit constant ζ_{SO} in the d -valence shells of some transition metals. Data from Landolt-Börnstein database and [160] (3d), from [19, 161] (4d) and from [162] (5d)

of a cubic crystal field splits further the six-fold multiplet. Indeed, the spin-orbit interaction in the cubic basis (e_g and t_{2g} in green and light green respectively in Fig. 2) can be reduced to two five-dimensional submatrices:

$$\left(\begin{array}{ccc|cc} 0 & -i & i & \sqrt{3} & -1 \\ i & 0 & -1 & -i\sqrt{3} & -i \\ -i & -1 & 0 & 0 & -2i \\ \hline \sqrt{3} & i\sqrt{3} & 0 & 0 & 0 \\ -1 & i & 2i & 0 & 0 \end{array} \right) \cdot \frac{\zeta_{SO}}{2} \quad \text{and} \quad \left(\begin{array}{ccc|cc} 0 & i & i & -\sqrt{3} & 1 \\ -i & 0 & 1 & -i\sqrt{3} & -i \\ -i & 1 & 0 & 0 & 2i \\ \hline -\sqrt{3} & i\sqrt{3} & 0 & 0 & 0 \\ 1 & i & -2i & 0 & 0 \end{array} \right) \cdot \frac{\zeta_{SO}}{2} \quad (5)$$

in the bases $\{d_{xz} \uparrow, d_{yz} \uparrow, d_{xy} \downarrow, d_{3z^2-r^2} \downarrow, d_{x^2-y^2} \downarrow\}$ and $\{d_{xz} \downarrow, d_{yz} \downarrow, d_{xy} \uparrow, d_{3z^2-r^2} \uparrow, d_{x^2-y^2} \uparrow\}$ respectively. After diagonalization, the total angular momentum J remains a good quantum number, contrary to j_z/m_j and one gets the following fine structure:

- a first quartet of $J = 5/2$ states (in red) with an energy

$$\varepsilon_{\frac{5}{2}+} = \frac{1}{4} (2\Delta - \zeta_{SO}) + \frac{1}{4} \sqrt{(2\Delta + \zeta_{SO})^2 + 24\zeta_{SO}^2}$$

- a doublet of $J = 5/2$ states (in yellow) of energy

$$\varepsilon_{\frac{5}{2}-} = +2 \frac{\zeta_{SO}}{2}$$

- a quartet of $J = 3/2$ states (in light blue) with an energy

$$\varepsilon_{\frac{3}{2}} = \frac{1}{4} (2\Delta - \zeta_{SO}) - \frac{1}{4} \sqrt{(2\Delta + \zeta_{SO})^2 + 24\zeta_{SO}^2}$$

In the limit of strong crystal field ($\Delta \gg \zeta_{SO}$), the $J = 5/2$ doublet (in yellow) remains invariant while the higher-energy quartet will tend to the usual e_g states and the lower-energy $J = 3/2$ quartet will be composed of t_{2g} states only, with an energy of $-\zeta_{SO}/2$.

Since the SOC-matrix restricted to the t_{2g} subspace is exactly the opposite of the SOC-matrix of the p -states of a free atom, one usually labels these latter states by a j_{eff} quantum number in analogy with the $p_{\frac{1}{2}}$ and $p_{\frac{3}{2}}$ multiplets, leading to the expressions given in Eq. (1) and (2). We point out that the $j_{\text{eff}}=1/2$ doublet arises from the interplay of both cubic symmetry and SOC, whatever the strength of the crystal field. The corresponding eigenstates can indeed be written:

$$\begin{aligned} \left| \frac{1}{2}, +\frac{1}{2} \right\rangle &= +\frac{1}{\sqrt{3}} \left(|d_{yz}, \downarrow\rangle + i |d_{xz}, \downarrow\rangle \right) + \frac{1}{\sqrt{3}} |d_{xy}, \uparrow\rangle = \frac{i}{\sqrt{6}} \left(\sqrt{5} \left| \frac{5}{2}, -\frac{3}{2} \right\rangle - \left| \frac{5}{2}, \frac{5}{2} \right\rangle \right) \\ \left| \frac{1}{2}, -\frac{1}{2} \right\rangle &= +\frac{1}{\sqrt{3}} \left(|d_{yz}, \uparrow\rangle - i |d_{xz}, \uparrow\rangle \right) - \frac{1}{\sqrt{3}} |d_{xy}, \downarrow\rangle = \frac{i}{\sqrt{6}} \left(\sqrt{5} \left| \frac{5}{2}, \frac{3}{2} \right\rangle - \left| \frac{5}{2}, -\frac{5}{2} \right\rangle \right) \end{aligned}$$

(where the right-hand side is written using the J, m_J quantum numbers). This may explain the robustness of this doublet in spin-orbit compounds [163]. However, the splitting between the $j_{\text{eff}}=1/2$ and $j_{\text{eff}}=3/2$ multiplets follows the inverse Landé interval rule (with the $j_{\text{eff}}=1/2$ above the $j_{\text{eff}}=3/2$ states) only in the strong crystal field limit.

3 Interplay of spin-orbit interaction and Coulomb correlations from first principles

3.1 DFT+DMFT calculations with spin-orbit coupling

Combined density functional theory (DFT) and dynamical mean-field theory (DMFT), as pioneered in [164, 165] (for a review, see [166, 167]), has made correlated electron systems accessible to first principles calculations. Over the years, various classes of systems ranging from transition metals [168–171], their oxides [11, 172–177], sulphides [178, 179], pnictides [4, 9, 180, 181], rare earths [182–184] and their compounds [185–188], including heavy fermions [189, 190], actinides [191, 192] and their compounds [193, 194] to organics [195], correlated semiconductors [196, 197], and correlated surfaces and interfaces [198–200] have been studied with great success. Besides intensive methodological developments (see e.g. [2, 3, 201–205]), recent research activities continue to extend to new materials classes. In this context, also 4d and 5d oxides have come into focus [21, 22, 62]. In this section, we review the technical aspects related to combined DFT+DMFT calculations in the presence of spin-orbit interactions. Since the applications we later focus on are 4d and 5d oxides in their *paramagnetic* phases, we restrict the discussion to this case.

In DMFT, a local approximation is made to the many-body self-energy which can then be calculated from an effective atom problem, subject to a self-consistency condition (see Fig. 3).

The notion of locality is understood in the sense of many-body theory as a site-diagonal form, with respect to atomic sites after representing the Hamiltonian in an atom-centered Wannier-type basis $|w_{\ell m}^{\alpha, \sigma}\rangle$, where the index α labels the atom in the unit-cell, (ℓ, m) the angular momentum quantum numbers of the atomic orbital and σ the spin degree of freedom. Different choices are possible for the construction of the atom-centered orbitals, and the work reviewed here is based on the construction of projected atomic orbitals subject to a subsequent orthonormalisation procedure [180].

The DMFT self-consistency cycle links the local effective atom problem to the electronic structure of the solid, via the transformation matrix from the Kohn-Sham states $|\psi_{\mathbf{k}\nu}^{\sigma}\rangle$, labelled by their momentum \mathbf{k} their band index ν and their spin σ , to the resulting Wannier-like local orbitals $|w_{\ell m}^{\alpha, \sigma}\rangle$. These key quantities are called *projectors* and denoted $P_{\ell m, \nu}^{\alpha, \sigma}(\mathbf{k})$.

The main advantage of projector-based implementations of DFT+DMFT (see e.g. [180, 207, 208]) is that not only the DFT-based part of the calculations but also the determination of the local Green’s function, used within the DMFT self-consistency condition, can be performed in any convenient basis set, and notably in the one used in the respective DFT code. Since the transformation of the DFT Hamiltonian matrix in that basis into the Kohn-Sham eigenset $|\psi_{\mathbf{k}\nu}^{\sigma}\rangle$ is known, it is sufficient to further determine the projections of the Kohn-Sham eigenstates onto

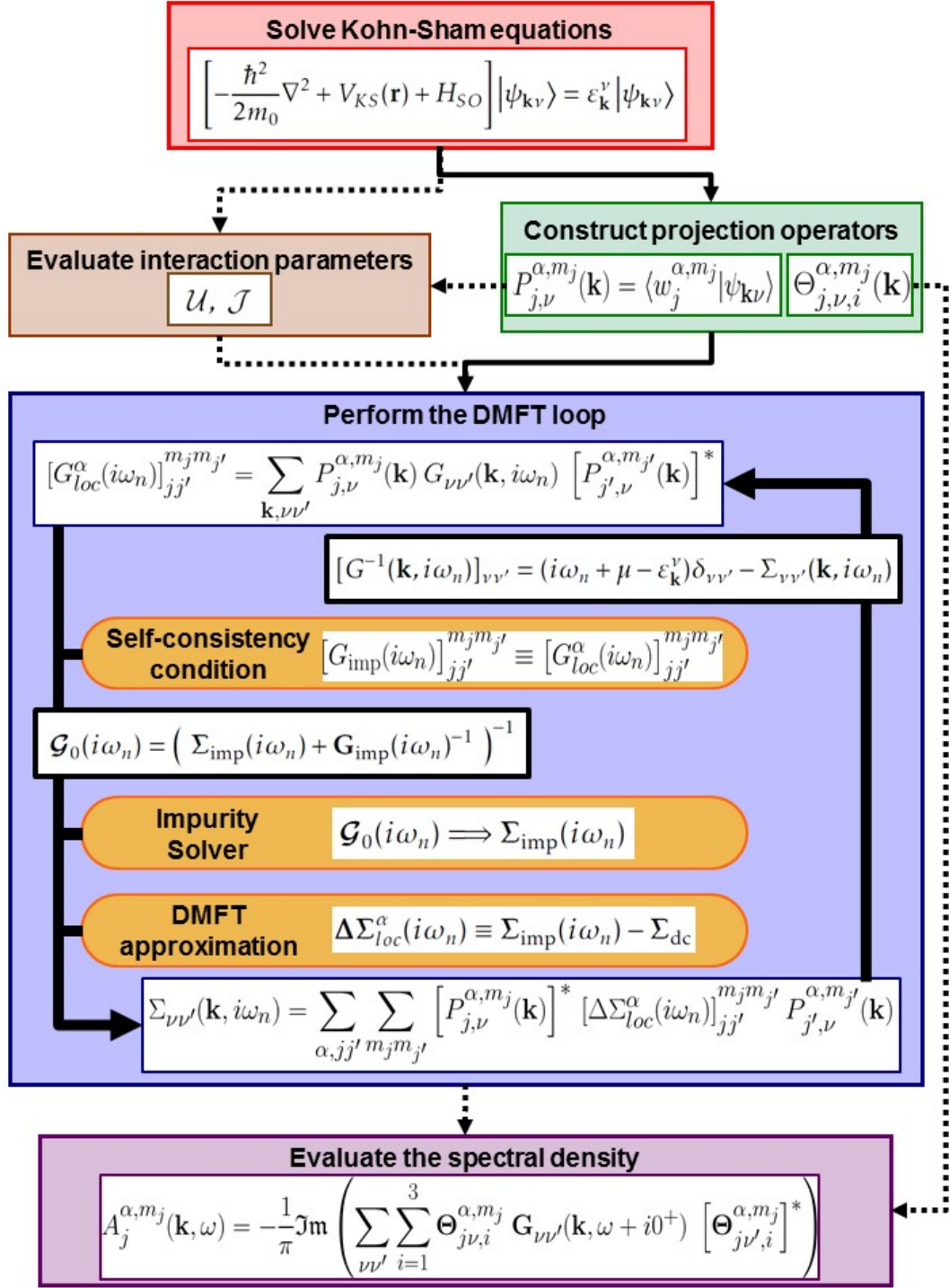


Figure 3: Projector-based implementation of DFT+DMFT for calculations including spin-orbit coupling in the Kohn-Shame equations. Once the Kohn-Shame eigenstates $|\psi_{\mathbf{k}\nu}\rangle$ are known, their projections $P_{j,\nu}^{\alpha,m_j}(\mathbf{k})$ to the correlated Wannier-like orbitals $|w_j^{\alpha,m_j}\rangle$ are calculated. One can then build an effective local many-body atomic problem, subject to a self-consistency condition, which is solved using an impurity solver: this defines the DMFT loop (see Section 3.1). The interaction parameters can also be evaluated consistently using the projectors $P_{j,\nu}^{\alpha,m_j}(\mathbf{k})$ (see [206] and Section 3.3). After convergence of the DMFT cycle, the chemical potential is updated and the spectral function can be evaluated using partial projectors $\Theta_{j\nu,i}^{\alpha,m_j}(\mathbf{k})$ (see Appendix A).

the local orbitals $|w_{\ell m}^{\alpha, \sigma}\rangle$ used in the DMFT impurity problem. This is precisely the role of the projectors.

In [21], this construction was generalised to the case when spin is not a good quantum number any more, and implemented within the framework of the DFT+DMFT implementation of Ref. [180]. Nowadays, it is available within the TRIQS/DFTTools package [209] that links the Wien2k code [210] to DMFT. We give here the main lines of this generalisation of the projector-based DFT+DMFT formalism.

When taking into account SOC, the Kohn-Sham eigenstates $|\psi_{\mathbf{k}\nu}\rangle$ are built out of *both* spin-up and spin-down states – in a similar fashion as the previously introduced $j_{\text{eff}}=1/2$ and $j_{\text{eff}}=3/2$ atomic states. Nevertheless, we can still write them in the following Bloch form:

$$\begin{aligned}\psi_{\mathbf{k}\nu}(\mathbf{r}) &= \left[u_{\mathbf{k}\nu}^{\uparrow}(\mathbf{r}) + u_{\mathbf{k}\nu}^{\downarrow}(\mathbf{r}) \right] e^{i\mathbf{k}\cdot\mathbf{r}} \\ &= \phi_{\mathbf{k}\nu}^{\uparrow}(\mathbf{r}) + \phi_{\mathbf{k}\nu}^{\downarrow}(\mathbf{r}).\end{aligned}\tag{6}$$

where the index ν now runs over *both* spin and band indices. The state $|\phi_{\mathbf{k}\nu}^{\sigma}\rangle$ denotes the projection of the Kohn-Sham state onto its spin- σ contribution and is *not* an eigenstate of the Hamiltonian.

Using this decomposition, we can define the new projectors:

$$P_{\ell m, \nu}^{\alpha, \sigma}(\mathbf{k}) = \langle w_{\ell m}^{\alpha, \sigma} | \psi_{\mathbf{k}\nu} \rangle = \langle w_{\ell m}^{\alpha, \sigma} | \phi_{\mathbf{k}\nu}^{\sigma} \rangle\tag{7}$$

We define them in the standard complex basis, but allow for a basis transformation to quantum numbers j, m_j (like $j_{\text{eff}}=1/2$ and $j_{\text{eff}}=3/2$) afterwards by means of a unitary matrix transformation in the correlated ℓ -space:

$$P_{j, \nu}^{\alpha, m_j}(\mathbf{k}) = \sum_{m, \sigma} \mathcal{S}_{j, \ell m}^{m_j, \sigma} \langle w_{\ell m}^{\alpha, \sigma} | \psi_{\mathbf{k}\nu} \rangle = \sum_{m, \sigma} \mathcal{S}_{j, \ell m}^{m_j, \sigma} P_{\ell m, \nu}^{\alpha, \sigma}(\mathbf{k})\tag{8}$$

The main difference with the usual implementation where spin is a good quantum number is that there are now two projectors associated to each band index ν : $P_{\ell m, \nu}^{\alpha, \sigma}(\mathbf{k})$ with $\sigma = \uparrow, \downarrow$.

Using the decomposition (6) in the formulation of the self-consistency condition relating the lattice Green's function of the solid to the impurity model, the (inverse) Green's function of the solid is given by:

$$[G^{-1}(\mathbf{k}, i\omega_n)]_{\nu\nu'} = (i\omega_n + \mu - \varepsilon_{\mathbf{k}}^{\nu})\delta_{\nu\nu'} - \Sigma_{\nu\nu'}(\mathbf{k}, i\omega_n),\tag{9}$$

where $\varepsilon_{\mathbf{k}}^{\nu}$ are the (ν -dependent only) Kohn-Sham eigenvalues and $\Sigma_{\nu\nu'}(\mathbf{k}, i\omega_n)$ is the approximation to the self-energy obtained by the solution of the DMFT impurity problem. It is obtained by "mapping" the impurity self-energy to the local self-energy of the lattice and "upfolding" it as:

$$\Sigma_{\nu\nu'}(\mathbf{k}, i\omega_n) = \sum_{\alpha, jj'} \sum_{m_j m_{j'}} \left[P_{j, \nu}^{\alpha, m_j}(\mathbf{k}) \right]^* [\Delta \Sigma_{loc}^{\alpha}(i\omega_n)]_{jj'}^{m_j m_{j'}} P_{j', \nu'}^{\alpha, m_{j'}}(\mathbf{k}).\tag{10}$$

with

$$[\Delta \Sigma_{loc}^{\alpha}(i\omega_n)]_{jj'}^{m_j m_{j'}} = [\Sigma_{\text{imp}}(i\omega_n)]_{jj'}^{m_j m_{j'}} - [\Sigma_{dc}]_{jj'}^{m_j m_{j'}}\tag{11}$$

Here, $\Sigma_{\text{imp}}(i\omega_n)$ is the impurity self-energy, expressed in the local orbitals, and Σ_{dc} is the double-counting correction. Consequently, the equations of the DMFT loop (see Figure 3) are formally the same as in the case without SOC but the computations now involve matrices which are double in size.

The local Green's function is obtained by projecting the lattice Green's function to the set of correlated orbitals and summing over the full Brillouin zone,

$$[G_{loc}^\alpha(i\omega_n)]_{jj'}^{m_j m_{j'}} = \sum_{\mathbf{k}, \nu\nu'} P_{j,\nu}^{\alpha, m_j}(\mathbf{k}) G_{\nu\nu'}(\mathbf{k}, i\omega_n) \left[P_{j',\nu'}^{\alpha, m_{j'}}(\mathbf{k}) \right]^*. \quad (12)$$

In practice, the summation over momenta is done in the irreducible Brillouin zone only, supplemented by a standard symmetrization procedure, using Shubnikov magnetic point groups [211, 212].

The DMFT equations are solved iteratively: starting from an initial local Green's function $G_{loc}^\alpha(i\omega_n)$ (obtained from the "pure" Kohn-Sham lattice Green's function using Eq. (12)), the Green's function $\mathcal{G}_0(i\omega_n)$ of the effective environment in the impurity model is constructed. The impurity model is solved, allowing to evaluate the local self-energy of the solid (cf. Eq. 10) and a new lattice Green's function $G(\mathbf{k}, i\omega_n)$. The latter can then be projected again onto the correlated subset and the cycle is repeated until convergence is reached.

3.2 Computation of the Wannier projectors within the augmented plane wave framework

The present implementation is within a full-potential linearized augmented plane wave (FLAPW) framework, as realised in the Wien2k package [210]. With respect to the existing DFT+DMFT implementation [180] in this context, the main changes concern the projection technique for building the correlated orbitals: as discussed above, one has to take care of the fact that spin is no longer a good quantum number, leading to the more general construction of localized "spin-orbitals". The necessary modifications in the construction of the projectors are reviewed in the following.

As in the case without SOC, we still use the Kohn-Sham states within a chosen energy window \mathcal{W} to form the Wannier-like functions that are treated as correlated orbitals, and the construction of the Wannier projectors is done in two steps. First, auxiliary Wannier projectors $\tilde{P}_{\ell m, \nu}^{\alpha, \sigma}(\mathbf{k})$ are calculated – separately for each $|\phi_{\nu \mathbf{k}}^\sigma\rangle$ term – from the following expression:

$$\begin{aligned} \tilde{P}_{\ell m, \nu}^{\alpha, \sigma}(\mathbf{k}) &= \langle u_\ell^{\alpha, \sigma}(E_1 \ell) Y_m^\ell | \psi_{\mathbf{k} \nu} \rangle \\ &= A_{\ell m}^{\nu \alpha}(\mathbf{k}, \sigma) + \sum_{n_{LO}=1}^{N_{LO}} c_{LO}^{\nu, \sigma} C_{\ell m}^{\alpha, LO} \mathcal{O}_{\ell m, \ell' m'}^{\alpha, \sigma}. \end{aligned} \quad (13)$$

A description of the augmented plane wave (APW) basis can be found in Ref. [180]. We use the same notations e.g. for the coefficients $A_{\ell m}^{\nu \alpha}(\mathbf{k}, \sigma)$ and the overlap matrix $\mathcal{O}_{\ell m, \ell' m'}^{\alpha, \sigma}$ as introduced there.

One performs an orthonormalisation step in order to get the Wannier projectors $P_{\ell m, \nu}^{\alpha, \sigma}(\mathbf{k})$. The

overlap matrix $[O(\mathbf{k})]_{(m\sigma),(m'\sigma')}^{\alpha,\alpha'}$ between the correlated ℓ orbitals is defined by:

$$[O(\mathbf{k})]_{(m\sigma),(m'\sigma')}^{\alpha,\alpha'} = \sum_{\nu=\nu_{\min}(\mathbf{k})}^{\nu_{\max}(\mathbf{k})} \tilde{P}_{\ell m,\nu}^{\alpha,\sigma}(\mathbf{k}) \tilde{P}_{\ell m',\nu}^{\alpha',\sigma'*}(\mathbf{k}). \quad (14)$$

leading to the final projectors:

$$P_{\ell m,\nu}^{\alpha,\sigma}(\mathbf{k}) = \sum_{\alpha',m',\sigma'} \left\{ [O(\mathbf{k})]^{-1/2} \right\}_{(m\sigma),(m'\sigma')}^{\alpha,\alpha'} \tilde{P}_{\ell m',\nu}^{\alpha',\sigma'}(\mathbf{k}), \quad (15)$$

which are then further transformed into a j, m_j basis as described above (cf. Eq. (8)).

3.3 Effective local Coulomb interactions from first principles

Hubbard interactions U – obtained as the static ($\omega = 0$) limit of the onsite matrix element $\langle |W^{\text{partial}}| \rangle$ within the “constrained random phase approximation” (cRPA) – have by now been obtained for a variety of systems, ranging from transition metals [213] to oxides [206, 214–217], pnictides [181, 218–220], f-electron elements [221] and compounds [188], to surface systems [222], and several implementations within different electronic structure codes and basis sets have been done, e.g. within linearized muffin tin orbitals [213, 223], maximally localized Wannier functions [214, 219, 224] (as elaborated in [225]), or localised orbitals constructed from projected atomic orbitals [206]. The implementation into the framework of the Wien2k package [206] made it possible that Hubbard U ’s be calculated for the same orbitals as the ones used in subsequent DFT+DMFT calculations, and, to our knowledge, Ref. [21] was indeed the first work using in this way consistently calculated Hubbard interactions in a DFT+DMFT calculation. Systematic calculations investigating the basis set dependence for a series of correlated transition metal oxides revealed furthermore interesting trends, depending on the choice of the low-energy subspace. In contrast to common belief until then, Hubbard interactions increase for example with the principal quantum number when low-energy effective models encompassing only the t_{2g} orbitals are employed. These trends can be rationalised by two counteracting mechanisms, the increasing extension of the orbitals with increasing principal quantum number and the less efficient screening by oxygen states [206]. We will come back to this point below, in the context of the cRPA calculations for our target compounds.

In the following, we review the specificities involved when determining the Hubbard interactions for our target spin-orbit compounds. We hereby use the same notations as in [206].

We start from the standard Hubbard-Kanamori Hamiltonian H_{int} which allows us to describe the interactions between t_{2g} orbitals within a Hamiltonian restricted to the t_{2g} -space:

$$\begin{aligned} H_{\text{int}} &= \mathcal{U} \sum_m n_{m\uparrow} n_{m\downarrow} + \mathcal{U}' \sum_{m < n, \sigma} n_{m\sigma} n_{n\bar{\sigma}} \\ &+ (\mathcal{U}' - \mathcal{J}) \sum_{m < n, \sigma} n_{m\sigma} n_{n\sigma} \\ &- \mathcal{J} \sum_{m < n, \sigma} \left[c_{m\sigma}^\dagger c_{m\bar{\sigma}} c_{n\bar{\sigma}}^\dagger c_{n\sigma} + c_{m\sigma}^\dagger c_{m\bar{\sigma}}^\dagger c_{n\sigma} c_{n\bar{\sigma}} \right] \end{aligned} \quad (16)$$

where \mathcal{U} is the intra-orbital Coulomb repulsion term and $\mathcal{U}' (= \mathcal{U} - 2\mathcal{J}$ with cubic symmetry) the interorbital Coulomb interaction which is reduced by Hund's exchange \mathcal{J} . (m and n run over the three t_{2g} orbitals and σ stands for the spin).

To draw the link between the cRPA calculations and this model Hamiltonian, the terms \mathcal{U} , \mathcal{U}' and \mathcal{J} are understood as the Slater-symmetrized effective interactions in the t_{2g} subspace, related to the Slater integrals F^0 , F^2 and F^4 as:

$$\mathcal{U} = F^0 + \frac{4}{49}(F^2 + F^4) \quad \text{and} \quad \mathcal{J} = \frac{3}{49}F^2 + \frac{20}{441}F^4 \quad (17)$$

The last relation $\mathcal{U}' = F^0 - \frac{2}{49}F^2 - \frac{4}{441}F^4$ is redundant since $\mathcal{U}' = \mathcal{U} - 2\mathcal{J}$.

One now transforms H_{int} into the j_{eff} basis using the unitary matrix transformation $\mathcal{S}_{j,lm}^{m_j,\sigma}$. Keeping only density-density terms, H_{int} becomes:

$$H_{\text{int}} = \frac{1}{2} \sum_{j,m_j} \sum_{j',m_{j'}} U_{jj'}^{m_j m_{j'}} n_{j,m_j} n_{j',m_{j'}} \quad (18)$$

Here, the index j is a shortcut notation for the $j_{\text{eff}} = \{3/2, 1/2\}$ quantum number and $m_j = \{\pm 3/2, \pm 1/2\}$. The reduced interaction matrix $U_{jj'}^{m_j m_{j'}}$ has the following form:

$$U_{jj'}^{m_j m_{j'}} = U_{jj'}^{\bar{m}_j \bar{m}_{j'}} = \begin{pmatrix} 0 & \mathcal{U} - 2\mathcal{J} & \mathcal{U} - \frac{5}{3}\mathcal{J} \\ \mathcal{U} - 2\mathcal{J} & 0 & \mathcal{U} - \frac{7}{3}\mathcal{J} \\ \mathcal{U} - \frac{5}{3}\mathcal{J} & \mathcal{U} - \frac{7}{3}\mathcal{J} & 0 \end{pmatrix} \quad (19)$$

$$U_{jj'}^{m_j \bar{m}_{j'}} = U_{jj'}^{\bar{m}_j m_{j'}} = \begin{pmatrix} \mathcal{U} - \frac{4}{3}\mathcal{J} & \mathcal{U} - \frac{8}{3}\mathcal{J} & \mathcal{U} - \frac{8}{3}\mathcal{J} \\ \mathcal{U} - \frac{8}{3}\mathcal{J} & \mathcal{U} - \mathcal{J} & \mathcal{U} - \frac{7}{3}\mathcal{J} \\ \mathcal{U} - \frac{8}{3}\mathcal{J} & \mathcal{U} - \frac{7}{3}\mathcal{J} & \mathcal{U} - \mathcal{J} \end{pmatrix} \quad (20)$$

We use the standard convention that \bar{m}_j denotes $-m_j$, as usually done for spin degree of freedom. The ordering of the orbitals $|j, |m_j|\rangle$ is: $|1/2, 1/2\rangle, |3/2, 1/2\rangle, |3/2, 3/2\rangle$, $j_{\text{eff}}=1/2$ and $j_{\text{eff}}=3/2$ blocks are emphasized to ease the reading of the matrices.

3.4 Technicalities of the DMFT calculation

For the solution of the quantum impurity problem we apply the continuous-time quantum Monte Carlo method (CTQMC) in the strong-coupling formulation [226]. We are able to perform calculations at room temperature ($\beta = 1/k_B T = 40 \text{ eV}^{-1}$) with reasonable numerical effort. In our calculations, we use typically around 16×10^6 Monte Carlo sweeps and 28 \mathbf{k} -points in the irreducible Brillouin zone.

Since the CTQMC solver computes the Green's function on the imaginary-time axis, an analytic continuation is needed in order to obtain results on the real-frequency axis. A continuation of the impurity self-energy using a stochastic version of the maximum entropy method [227] yields real and imaginary parts of the retarded self-energy. From those, we calculate the momentum-resolved spectral function $A(\mathbf{k}, \omega)$ using partial projectors introduced in Appendix A.

During the calculations we use the Fully Localized Limit (FLL) expression for the double-counting:

$$\Sigma_{jj'}^{dc} = \left[U(N_c - \frac{1}{2}) - J(\frac{1}{2}N_c - \frac{1}{2}) \right] \delta_{jj'} \quad (21)$$

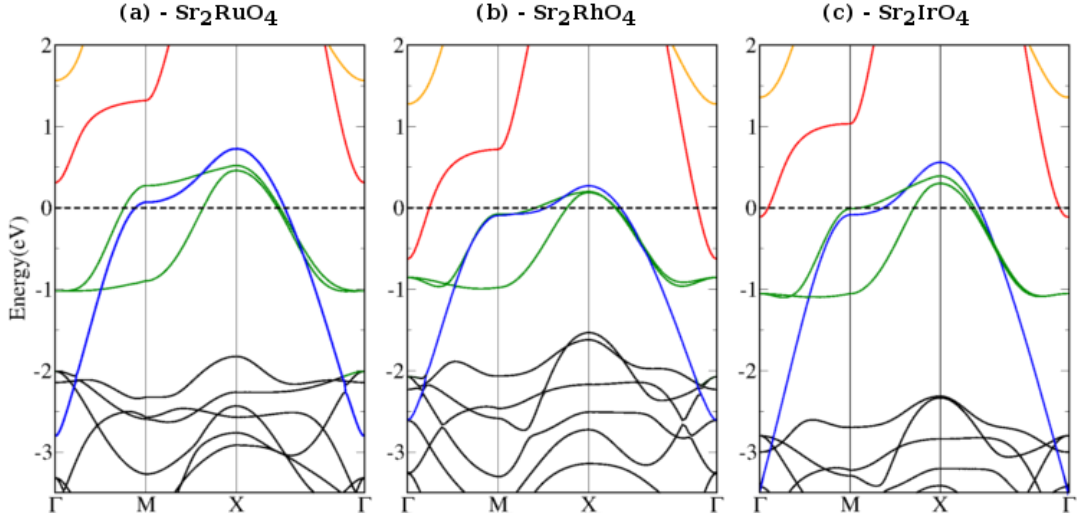


Figure 4: Kohn-Sham band structures of Sr_2RuO_4 (a) Sr_2RhO_4 (b) and Sr_2IrO_4 (c) within LDA (and without spin-orbit coupling), artificially assuming that both Sr_2RhO_4 and Sr_2IrO_4 crystallize in the same K_2NiF_4 structure as their Ru-counterpart. For Sr_2RuO_4 , we use the lattice parameters at 300 K given in [230]. The t_{2g} -dominated bands are plotted in green (d_{xy}) and blue (d_{xz} and d_{yz}) while the e_g bands are in red ($d_{x^2-y^2}$) and yellow ($d_{3z^2-r^2}$), the O-2p states in black.

where j and j' run over the j_{eff} states and N_c is the total occupancy of the orbitals. (Since each orbital is doubly degenerate in m_j , $N_c/2$ is used in the term containing J). Moreover, we neglect the off-diagonal terms in the local Green's functions (particularly, we neglect the term between the $j_{\text{eff}}=1/2$ and the $j_{\text{eff}}=3/2$ $|m_j| = 1/2$ which we checked to be two orders of magnitude smaller than the diagonal terms, in the chosen basis).

4 Electronic structure of Sr_2IrO_4 and Sr_2RhO_4

4.1 Electronic structure of Sr_2IrO_4 and Sr_2RhO_4 within DFT-LDA

The Kohn-Sham band structures of Sr_2IrO_4 and Sr_2RhO_4 within the local density approximation and in the presence of spin-orbit coupling (LDA+SO) are represented in Fig. 5-(d) and (e). For Sr_2IrO_4 , we use the lattice parameters measured at 295 K in [228], and for Sr_2RhO_4 those measured at 300 K in [229].

The LDA+SO band structures for Sr_2IrO_4 and Sr_2RhO_4 are very similar, as a consequence of both, the structural similarity and the key role of spin-orbit coupling in these compounds. The e_g -states ($d_{x^2-y^2}$ in red and $d_{3z^2-r^2}$ in yellow) start at about 1 to 1.5 eV, and are fully separated from the t_{2g} -manifold which lies around the Fermi level and overlaps at lower energies with the oxygen 2p-states (black). Given the t_{2g}^5 filling and the four-atom unit cell of both compounds, a metallic solution is obtained within LDA for both Sr_2RhO_4 and Sr_2IrO_4 – at variance with experiments for Sr_2IrO_4 . Among the t_{2g} -manifold (in green), only the four highest-lying bands, highlighted in blue, cross the Fermi level: this is suggestive of the existence of a separated half-filled $j_{\text{eff}}=1/2$ -derived band, which – within a four-atom unit cell – corresponds to a quartet of bands at each k-point. We stress however that the true picture is much more subtle: in

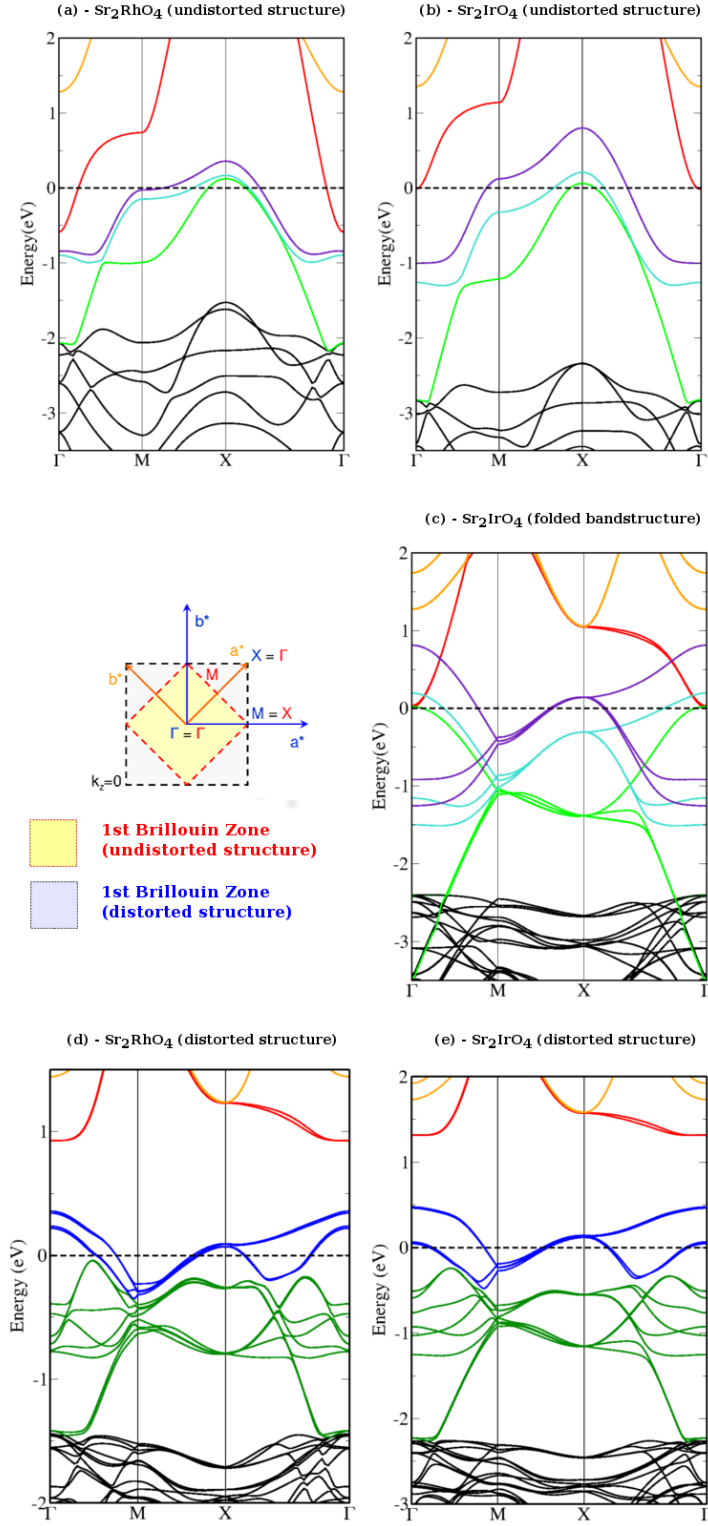


Figure 5: Kohn-Sham band structures within LDA+SO of Sr_2RhO_4 and Sr_2IrO_4 assuming that they crystallize without distortions in a K_2NiF_4 structure (a-b), of Sr_2IrO_4 in a supercell containing 4 "undistorted" unit-cells (c) and of "real" Sr_2RhO_4 and Sr_2IrO_4 (d-e). The reduction of the first Brillouin zone, when the crystal symmetry is lowered, is also shown. The e_g states are in yellow ($d_{3z^2-r^2}$) and red ($d_{x^2-y^2}$). In the t_{2g} manifold, in purple the $j_{\text{eff}}=1/2$ in light blue the $j_{\text{eff}}=3/2$ $m_j = 3/2$ and in green the $j_{\text{eff}}=3/2$ $m_j = 1/2$. In black, the O-2p states.

fact, $j_{\text{eff}}=1/2$ and $j_{\text{eff}}=3/2$ overlap (see the band structure between the Γ and the M-point for instance) and the identification of the upper four bands as the $j_{\text{eff}}=1/2$ states is too simplistic. We will come back to this point below.

To get a better understanding of the Kohn-Sham band structures of Sr_2RhO_4 and Sr_2IrO_4 , we study artificial compounds where both the structural distortions and the spin-orbit coupling have been switched off. Fig. 4-(b) and (c) depict the LDA band structure of such "idealized undistorted Sr_2RhO_4 and Sr_2IrO_4 ". Neglecting the rotation of about 10° of their IrO_6 and RhO_6 octahedra around the c -axis leads to a K_2NiF_4 -type crystal structure, like in Sr_2RuO_4 , the well-known LDA band structure of which is plotted in Fig. 4-(a).

The similarity of the three band structures is obvious. Around the Fermi level, one distinguishes the three t_{2g} bands. The d_{xy} -band (green) reaches out to lower energies and overlaps with the oxygen $2p$ -states (black). The e_g -states ($d_{x^2-y^2}$ in red and $d_{3z^2-r^2}$ yellow), higher in energy, cut the Fermi level in both Sr_2IrO_4 and Sr_2RhO_4 due the additional electron remaining in the d -manifold, contrary to Sr_2RuO_4 , which has actually a mere t_{2g}^4 -filling. The larger extension of the $5d$ orbitals (cf. Fig 1) explains the wider bandwidth observed for Sr_2IrO_4 in comparison to Sr_2RhO_4 : the d_{xy} band reaches the value of -3.5 eV in Γ , while it remains above -3 eV for the $4d$ counterparts. Another consequence of this wider extension is the stronger hybridization between the $5d$ states with the oxygen p -states, which are located 1 eV lower in energy in Sr_2IrO_4 than in the $4d$ -TMOs.

Re-introducing the effects of the spin-orbit coupling in Sr_2RhO_4 and Sr_2IrO_4 (but without considering the structural distortions) modifies these Kohn-Sham band structures to those shown in Fig 5-(a) and (b). The t_{2g} bands are the most affected, while the e_g bands are slightly shifted as a consequence of the topological change in the t_{2g} manifold. A detailed study of the character of these band structures confirms the decoupling between e_g and t_{2g} states (see also Refs. [19, 20]). The cubic crystal field at stake in these compounds is indeed much larger than the energy scale associated to the spin-orbit coupling of about $\zeta_{\text{SO}} \approx 0.4$ eV and $\zeta_{\text{SO}} \approx 0.2$ eV for Sr_2IrO_4 and Sr_2RhO_4 respectively.

The j_{eff} picture is thus justified in both, Sr_2IrO_4 and Sr_2RhO_4 : the t_{2g} orbitals split into a quartet of $j_{\text{eff}}=3/2$ states and a higher lying doublet $j_{\text{eff}}=1/2$. Each state is doubly degenerate in $\pm m_j$ – since we observe the system in its paramagnetic phase at room temperature and the crystal structure has a center of inversion. Therefore we still refer to them as the " $j_{\text{eff}}=1/2$ band" and the two " $j_{\text{eff}}=3/2$ bands" in the following. The three j_{eff} bands can easily be identified: the $j_{\text{eff}}=1/2$ one (light green) lies above the two $j_{\text{eff}}=3/2$ ones ($m_j = 3/2$ in light blue and $m_j = 1/2$ in violet). The three j_{eff} bands are well-separated all along the \mathbf{k} -path, and more generally in the whole Brillouin zone. Since the spin-orbit coupling is twice smaller in Sr_2RhO_4 , the splitting between the j_{eff} bands is reduced by a factor of 2, as one can see for instance at X or Γ .

To draw the link between the "undistorted" band structures and the realistic ones, we plot in Fig 5-(c) the LDA+SO band structure of the *undistorted* Sr_2IrO_4 in a supercell containing four unit cells. Each band is now folded four times and we provide a scheme of the two first Brillouin Zones in the $\mathbf{k}_z = 0$ plane to understand the correspondence between the high-symmetry points of each structure.

Comparing Fig 5-(c) and (e) highlights the key role of the structural distortion in Sr_2IrO_4 : an

hybridisation between two neighboring Ir d_{xy} and $d_{x^2-y^2}$ orbitals via the in-plane oxygens is now allowed and pushes the t_{2g} and e_g bands apart. Another consequence of the distortions is the general narrowing of the j_{eff} bandwidth, which is of crucial importance to drive the compound insulating, as we will see below.

Finally, comparing Fig 5-(c) and (e) gives more insights into the nature of the four highest-lying bands (blue) of Fig 5-(e). While along the $M - X$ direction, each quartet of j_{eff} bands remain well-separated, $j_{\text{eff}}=1/2$ and $j_{\text{eff}}=3/2$ overlap in the other direction $\Gamma - M$ and $M - X$. As a result, the $j_{\text{eff}}=3/2$ bands cross the Fermi-level closest to the Γ -point, while the other crossings are due to the $j_{\text{eff}}=1/2$ bands. The identification of the upper four bands in Sr_2IrO_4 as "pure" $j_{\text{eff}}=1/2$ states is thus too simplistic, implying the need for a Hamiltonian containing more than one orbital in a realistic calculation.

The same mechanisms are at stake in Sr_2RhO_4 even though we do not display the orbital characters here: the four highest-lying bands, highlighted in blue in Fig. 5-(d) exhibit a mixed character of type $j_{\text{eff}}=1/2$ and $j_{\text{eff}}=3/2$. Moreover, thanks to the distortions which allow the opening of a gap between t_{2g} and e_g bands, the LDA+SO Fermi surface becomes qualitatively similar to the experimental one: as shown in Fig. 8-(a), they both contain three closed contours : a circular hole-like α -pocket around Γ , a lens-shaped electron pocket β_M and a square-shaped electron pockets β_X . However the striking discrepancies in the size of the pockets point out a subtle deficiency of the LDA for Sr_2RhO_4 [19, 20].

4.2 Wannier functions

We have derived the Wannier functions associated to the j_{eff} manifold for both Sr_2IrO_4 and Sr_2RhO_4 , using the framework introduced in section 3.1. Because of the mixed character of the four bands that cross the Fermi level in Sr_2IrO_4 and Sr_2RhO_4 , the local effective atomic problem used in the DMFT cycle must contain the three j_{eff} orbitals and thus accomodate five electrons. We construct Wannier functions for the j_{eff} orbitals from the LDA+SO band structure of Sr_2IrO_4 and Sr_2RhO_4 , using an energy window $[-3.0, 0.5]$ eV for Sr_2IrO_4 and an energy window $[-2.67; 0.37]$ eV for Sr_2RhO_4 .

Fig. 6 and 7 depict the projection of these Wannier functions on the LDA+SO band structure. The similarities between Fig 6 and Fig 5-(c) are numerous, thus confirming our previous band character analysis. Tab. 5 gives the decomposition of these local Wannier functions on the t_{2g} manifold and their respective occupation.

To obtain deeper insights into the nature of these Wannier orbitals, Tab. 4 gives the coefficients of the local Wannier orbitals obtained from the LDA+SO band structure of "undistorted" Sr_2IrO_4 using an energy window $[-3.5, 0.8]$ eV. The results agree well with the standard j_{eff} picture (cf. Eq. (1) and (2)) in both modulus and phase. Discrepancies are mostly due to the elongation of the IrO_6 along the c -axis, which introduces an additional tetragonal field between the t_{2g} states. This effect also explains the lifting of the degeneracy of the two $j_{\text{eff}}=3/2$ ($m_j = \pm 1/2$ and $m_j = \pm 3/2$) states and implies the reason why the $j_{\text{eff}}=1/2$ is slightly more than half-filled.

Because of the hydridization between the d_{xy} and $d_{x^2-y^2}$ orbitals in the distorted structures, we had to define in practice "effective $j_{\text{eff}}=1/2$ and $j_{\text{eff}}=3/2$ $|m_j| = 1/2$ states", which remain

"undistorted" Sr_2IrO_4	$\left \frac{1}{2}, \pm\frac{1}{2}\right\rangle$	$\left \frac{3}{2}, \pm\frac{1}{2}\right\rangle$	$\left \frac{3}{2}, \pm\frac{3}{2}\right\rangle$
$ d_{xy}\uparrow\downarrow\rangle$	± 0.6605	$+0.7508$	0
$ d_{xz}\uparrow\downarrow\rangle$	$\pm 0.5309\ i$	$-0.4670i$	$-0.7071\ i$
$ d_{yz}\uparrow\downarrow\rangle$	$+ 0.5309$	∓ 0.4670	∓ 0.7071
occupation (LDA+SO)	1.20	1.92	1.86

Table 4: Coefficients and occupation of the j_{eff} Wannier orbitals in "undistorted" Sr_2IrO_4 . The discrepancy between these coefficients and those given in Eq. (1) and (2) are due to the small elongation of the octahedra along the c -axis.

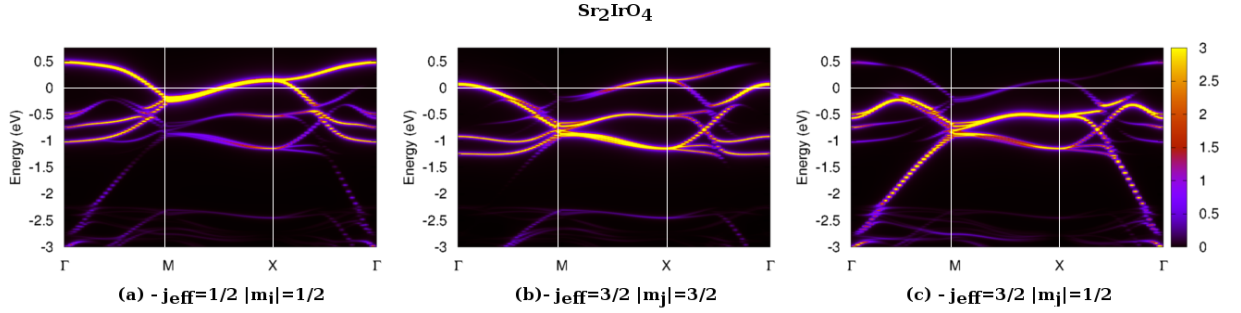


Figure 6: LDA+SO band structure of Sr_2IrO_4 , projected on the $j_{\text{eff}}=1/2$ (left panel), $j_{\text{eff}}=3/2\ |m_j|=3/2$ (middle), and $j_{\text{eff}}=3/2\ |m_j|=1/2$ (right panel) spin-orbitals.

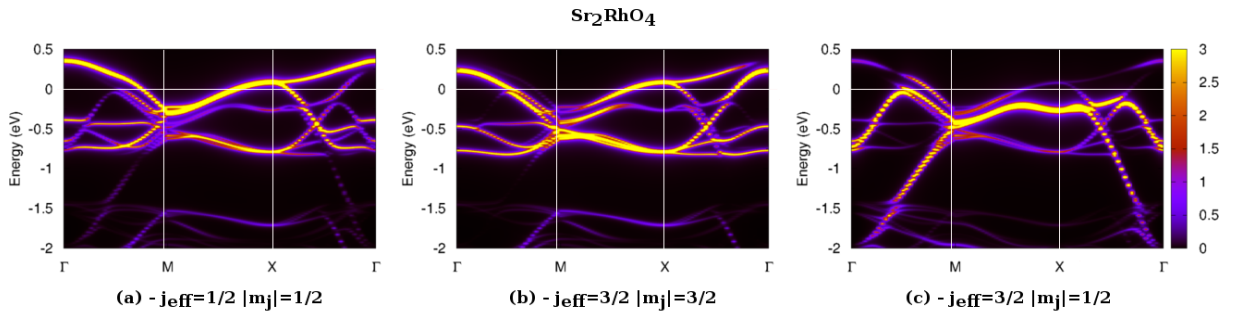


Figure 7: LDA+SO band structure of Sr_2RhO_4 , projected on the $j_{\text{eff}}=1/2$ (left panel), $j_{\text{eff}}=3/2\ |m_j|=3/2$ (middle), and $j_{\text{eff}}=3/2\ |m_j|=1/2$ (right panel) spin-orbitals.

	Sr ₂ IrO ₄			Sr ₂ RhO ₄		
Wannier orbitals	$\left \frac{1}{2}, \pm\frac{1}{2}\right\rangle$	$\left \frac{3}{2}, \pm\frac{1}{2}\right\rangle$	$\left \frac{3}{2}, \pm\frac{3}{2}\right\rangle$	$\left \frac{1}{2}, \pm\frac{1}{2}\right\rangle$	$\left \frac{3}{2}, \pm\frac{1}{2}\right\rangle$	$\left \frac{3}{2}, \pm\frac{3}{2}\right\rangle$
$ d_{x^2-y^2} \uparrow\downarrow\rangle$	0.0388	0.0766	0	0.0100	0.0302	0
$ d_{xy} \uparrow\downarrow\rangle$	0.4499	0.8889	0	0.3153	0.9485	0
$ d_{xz} \uparrow\downarrow\rangle$	0.6309	0.3193	0.7071	0.6710	0.2231	0.7071
$ d_{yz} \uparrow\downarrow\rangle$	0.6309	0.3193	0.7071	0.6710	0.2231	0.7071
occupation (LDA+SO)	1.16	1.98	1.84	1.42	1.96	1.64
charge (LDA+SO+DMFT)	1.02	2.00	1.98	1.26	1.98	1.76

Table 5: Modulus of the coefficients of the j_{eff} Wannier orbitals in Sr₂IrO₄ and Sr₂RhO₄. The occupation within LDA+SO and within LDA+SO+DMFT of each atomic Wannier orbitals is also provided, showing how electronic correlations enhance the spin-orbital polarization.

close to the atomic j_{eff} picture but take into account a small amount of $d_{x^2-y^2}$ character (cf. Tab. 5). The coefficients have been calculated such that the density matrix of the local atomic problem is closest possible to diagonal form.[†] In addition to the hybridization, the construction of the "effective j_{eff} " takes also into account the tetragonal crystal field due to the elongation of the octahedra in each crystal structure: this explains the discrepancies with the standard coefficients given in Eq. (1) and (2). We note that the coefficients obtained for the $j_{\text{eff}}=1/2$ state of Sr₂IrO₄ are equivalent to those obtained in the AF phase in Ref. [139].

Finally, comparing the occupation of the orbitals in Tab. 4 and 5 highlights again the role of the hybridisation between the d_{xy} and $d_{x^2-y^2}$ orbitals which pushes the band $j_{\text{eff}}=3/2$ $|m_j| = 1/2$ further below the Fermi level close to Γ : as a result, the four bands that cross the Fermi level are formed only by the $j_{\text{eff}}=1/2$ and $j_{\text{eff}}=3/2$ $|m_j|=3/2$ orbitals and the $j_{\text{eff}}=1/2$ tend to be close to half-filling. Similar conclusions were drawn for the AF phase within a Variational Cluster Approximation (VCA) approach in Ref. [140]. Similar conclusions hold for Sr₂RhO₄.

4.3 Effective Hubbard Interactions from cRPA

After defining the j_{eff} Wannier orbitals, we evaluate the local Coulomb interaction in the effective atomic problem within cRPA [206, 213], as explained in section 3.3. For reasons of computational resources, the cRPA calculations were performed in the case without distortions (without the rotations of the octahedra, hence considering only one formula-unit in a unit-cell) and without SOC. To mimic the effect of the distortions, the e_g states are shifted up to their energetic position in the presence of distortions. We find $\mathcal{U} = 2.54$ eV and $\mathcal{J} = 0.23$ eV for Sr₂IrO₄ and $\mathcal{U} = 1.94$ eV and $\mathcal{J} = 0.23$ eV for Sr₂RhO₄. These parameters lead to the following local

[†]With the obtained coefficients, the off-diagonal terms remaining in the local Greens functions between the $j_{\text{eff}}=1/2$ and $j_{\text{eff}}=3/2$ $|m_j| = 1/2$ are smaller than 0.05. In practice, the coefficients were chosen real. This can be done in the local problem since only density-density terms were kept for the interaction terms and off-diagonal terms of the density matrix were neglected.

interaction matrices for Sr_2IrO_4 :

$$U_{jj'}^{m_j m_{j'}} = \left(\begin{array}{c|cc} 0 & 2.08 & 2.21 \\ \hline 2.08 & 0 & 1.93 \\ 2.21 & 1.93 & 0 \end{array} \right) \quad U_{jj'}^{m_j \bar{m}_{j'}} = \left(\begin{array}{c|cc} 2.25 & 1.98 & 1.90 \\ \hline 1.98 & 2.38 & 2.03 \\ 1.90 & 2.03 & 2.31 \end{array} \right) \quad (22)$$

and for Sr_2RhO_4 :

$$U_{jj'}^{m_j m_{j'}} = \left(\begin{array}{c|cc} 0 & 1.48 & 1.66 \\ \hline 1.48 & 0 & 1.29 \\ 1.66 & 1.29 & 0 \end{array} \right) \quad U_{jj'}^{m_j \bar{m}_{j'}} = \left(\begin{array}{c|cc} 1.67 & 1.32 & 1.27 \\ \hline 1.32 & 1.86 & 1.46 \\ 1.27 & 1.46 & 1.71 \end{array} \right) \quad (23)$$

where the values are in eV and the ordering of the $|j, |m_j|\rangle$ orbitals is: $|1/2, 1/2\rangle, |3/2, 1/2\rangle, |3/2, 3/2\rangle$ and \bar{m}_j denotes $-m_j$. We remind the reader that $U_{jj'}^{m_j m_{j'}} = U_{jj'}^{\bar{m}_j \bar{m}_{j'}}$ and $U_{jj'}^{m_j \bar{m}_{j'}} = U_{jj'}^{\bar{m}_j m_{j'}}$. Since we have used "effective j_{eff} " Wannier orbitals instead of the standard definition given in Eq. (1) and (2), some discrepancies with the formulae given in Eq. (19) and in [22] can be observed. Contrary to common belief, the Hubbard interactions are smaller in the $4d$ -TMO than in its $5d$ -counterpart. This might seem counterintuitive at first sight, since the $5d$ -orbitals are more extended than the $4d$ ones, but finds its explanation in more efficient screening in the $4d$ material: As shown in Fig. 5-(d) and (e), the hybridization between the Rh- $4d$ states and the O- $2p$ is weaker in Sr_2RhO_4 than in Sr_2IrO_4 . Correspondingly, the energetic position of the O- $2p$ bands is closer to the Fermi level by about 1 eV, and as a result, the Coulomb interactions are screened more efficiently in Sr_2RhO_4 than in Sr_2IrO_4 , explaining the observed trend.

4.4 Correlated electronic structure of Sr_2IrO_4 and Sr_2RhO_4

DFT+DMFT calculations following the procedure described in section 3.1 indeed find an insulating solution for Sr_2IrO_4 and a correlated metal for Sr_2RhO_4 [21], in agreement with experiment. The difference in these metallic versus insulating nature of Sr_2RhO_4 and Sr_2IrO_4 can be traced back to the different spin-orbital polarization in the three j_{eff} orbitals, which is enhanced by Coulomb correlations.

The occupations of the j_{eff} Wannier orbitals within LDA+SO and LDA+SO+DMFT are provided in Tab. 5. In Sr_2IrO_4 , one detects a considerable spin-orbital polarisation already at the LDA+SO level: the four $j_{\text{eff}}=3/2$ states are almost filled with $n_{3/2, |1/2|}=1.98$ and $n_{3/2, |3/2|}=1.84$ while the $j_{\text{eff}}=1/2$ states thus slightly exceed half-filling with $n_{1/2}=1.16$ (as in the "ideal undistorted" case). Taking into account Coulomb correlations within DMFT opens a gap of about 0.26 eV [21] and enhances the spin-orbital polarisation, such as to fill the $j_{\text{eff}}=3/2$ states entirely, leading to a half-filled $j_{\text{eff}}=1/2$ state. This is thus the celebrated " $j_{\text{eff}}=1/2$ -picture" [16], which comes out here as a result of the calculations, rather than being an input as in most model Hamiltonian calculations.

A different picture emerges for Sr_2RhO_4 according to Tab. 5: while the spin-orbital occupations display some polarisation at the LDA+SO level, the smaller SOC – and thus the smaller effective splitting between the j_{eff} bands – leads to a picture where only the $j_{\text{eff}}=3/2$ $|m_j| = 1/2$ state is entirely filled while both $j_{\text{eff}}=3/2$ $|m_j| = 3/2$ and $j_{\text{eff}}=1/2$ live at the Fermi level. This spin-orbital polarization is enhanced by Coulomb correlations – just as in Sr_2IrO_4 – but this

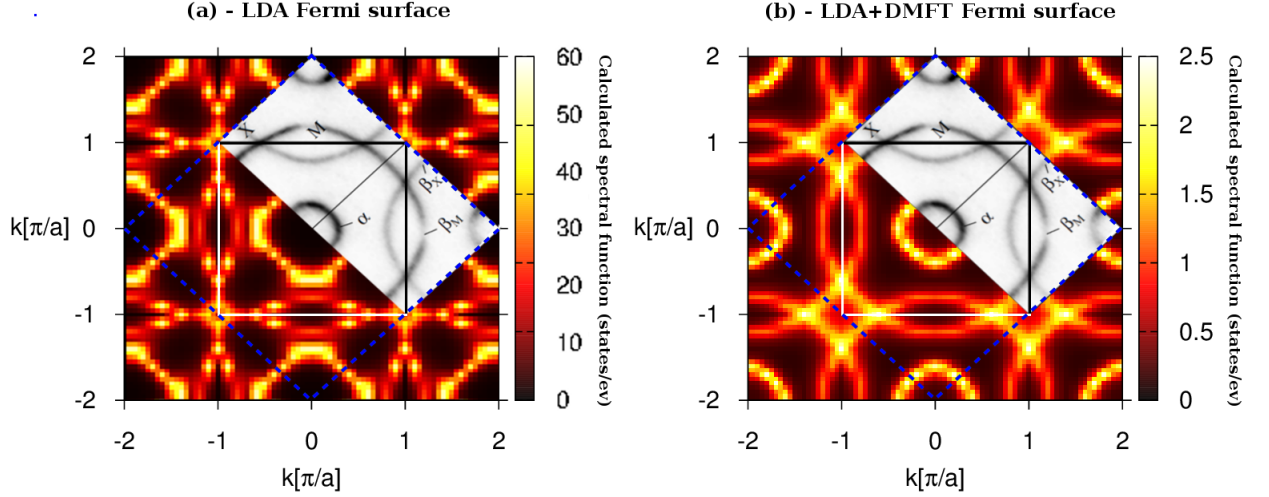


Figure 8: Calculated Fermi surface of Sr_2RhO_4 in the $\mathbf{k}_z = 0$ plane within LDA+SO (left panel) and LDA+SO+DMFT (right panel). Superimposed is the experimentally measured Fermi surface, from Ref. [120].

	α			β_X			β_M		
	LDA	DMFT	Exp.	LDA	DMFT	Exp.	LDA	DMFT	Exp.
FS volume A (% BZ)	18.4	10.1	6.1(4)	4.5	6.2	8.1(5)	10.0	7.6	7.4(4)
$\hbar v_F$ (eV.Å)	1.252	0.645	0.41(4)	1.260	0.674	0.55(6)	1.260	0.674	0.61(6)
m^* (m_e)	1.70	2.44	3.0(3)	0.83	1.83	2.6(3)	1.24	2.02	2.2(2)

Table 6: Comparison of the Fermi surface (FS) parameters evaluated within LDA+SO, within LDA+SO+DMFT and ARPES [120]. For each α , β_X and β_M pocket, the FS volume A is defined as a pourcentage of the two-dimensional-BZ volume (using the experimental lattice parameters ($a = 5.45$ Å)). The Fermi velocity $\hbar v_F$ is obtained from the slope of the band dispersion at the Fermi level. The cyclotron mass m^*/m_e is calculated using the same method as described in [120]: $m^* v_F = \hbar \sqrt{A/\pi}$.

enhancement is not enough to fill both $j_{\text{eff}}=3/2$ states entirely and obtain a half-filled $j_{\text{eff}}=1/2$ state. The higher effective degeneracy together with the smaller value of \mathcal{U} eventually leave Sr_2RhO_4 metallic.

4.5 Spectral properties of Sr_2RhO_4 : theory vs. experiment

We now turn to the calculated spectral function of the spin-orbital correlated metal Sr_2RhO_4 that we analyse in comparison to experiment.

Fig. 8 depicts the Fermi surface of Sr_2RhO_4 within LDA+SO (left panel) and LDA+SO+DMFT (right panel) in the $\mathbf{k}_z = 0$ plane, to which we superimpose the experimental measurement from [120]. Tab. 6 gives more quantitative insight to ease the comparison between the different topologies. All three Fermi surfaces, the two theoretical ones and the experimental one, are *qualitatively* similar with three closed contours : a circular hole-like α -pocket around Γ , a lens-shaped electron pocket β_M and a square-shaped electron pockets β_X . These two structures merge in the undistorted tetragonal zone (dashed blue line in Fig. 8) to a large electron-like

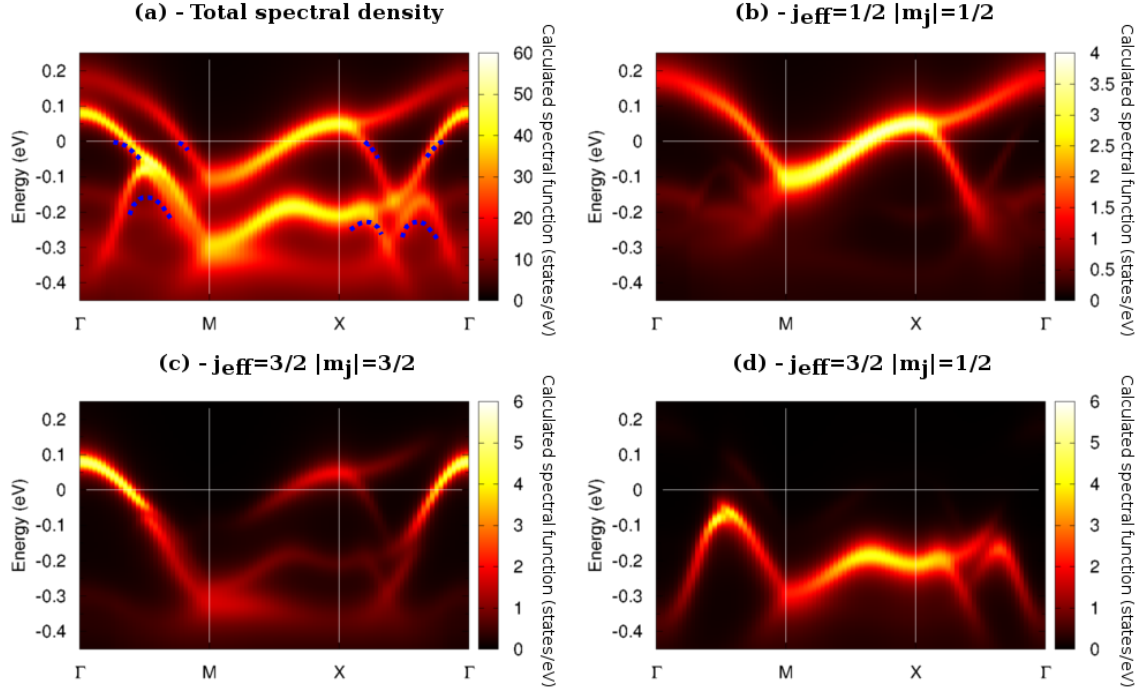


Figure 9: Calculated momentum-resolved spectral function of Sr_2RhO_4 within LDA+DMFT (a) and its orbital-resolved versions for the $j_{\text{eff}}=1/2$ states (b), the $j_{\text{eff}}=3/2$ $|m_j|=3/2$ (c) and the completely-filled $j_{\text{eff}}=3/2$ $|m_j|=1/2$ (d). The dashed blue line on panel (a) are the reproduction of the ARPES structure from [121]

pocket β .

Comparing Fig. 8-(a) and (b) highlights the key role of electronic correlations : they decrease the radius of the α pocket from $0.26 - 0.29 \text{ \AA}^{-1}$ to 0.21 \AA^{-1} and decrease the radius of the large β pocket from $0.69 - 0.72 \text{ \AA}^{-1}$ to $0.67 - 0.70 \text{ \AA}^{-1}$, thus enlarging the β_M and β_X pockets such that their volume are well-reproduced within LDA+SO+DMFT (cf. Tab 6). As a result, the agreement between LDA+SO+DMFT data and the experimental measurements becomes even quantitatively excellent.

To go further in the analysis, Fig. 9 depicts the momentum-resolved spectral function, as well as its orbital-resolved version. The completely filled $j_{\text{eff}}=3/2$ $|m_j|=1/2$ state is visible (panel d), as well as the partially filled character of the $j_{\text{eff}}=3/2$ $|m_j|=3/2$ (panel c) and $j_{\text{eff}}=1/2$ states (panel b). A detailed comparison with angle-resolved photoemission data from [121] (blue dashed line on the figure) shows that the band dispersion around the Fermi level is well-reproduced, while some discrepancies are observed for the structures experimentally observed along $\Gamma - X$ and $\Gamma - M$ at lower energy. These features, reminiscent of the $j_{\text{eff}}=3/2$ $|m_j|=1/2$ bands, are indeed located about 0.05 eV higher in energy in our calculated spectral function.

From Fig. 9-(b) and (c), one observes that the Fermi level is crossed by the renormalized $j_{\text{eff}}=3/2$ $|m_j|=3/2$ band at 0.20 \AA^{-1} along $\Gamma - X$ and at 0.21 \AA^{-1} along $\Gamma - M$, while the renormalized $j_{\text{eff}}=1/2$ band is responsible for all other crossings. This allows to label the hole-like α -pocket as

being of $j_{\text{eff}}=3/2$ $|m_j| = 3/2$ type, whereas the two other pockets β_M and β_X are mostly of type $j_{\text{eff}}=1/2$. Using the quasiparticle weight of each state ($Z_{1/2} = 0.535$ and $Z_{3/2,|3/2|} = 0.675$), we evaluate the Fermi velocity at each crossing along the path $[\Gamma M X \Gamma]$: we find a huge variation of the values depending on \mathbf{k} and give in Tab. 6 their mean value over the Brillouin zone. Finally, using the same method as described in [120], we evaluate the cyclotron mass m^*/m_e based on the approximate formula used there: $m^*\bar{v}_F = \hbar\sqrt{A/\pi}$. The DMFT results shown in Tab. 6 show a substantial improvement over DFT when compared to experiments.

5 The effective orbital degeneracy as a key quantity determining the correlation strength

In section 4.4, we have identified the spin-orbital polarization as a key factor to explain the different behavior of Sr_2RhO_4 and Sr_2IrO_4 .

In Sr_2IrO_4 , Coulomb correlations enhance the spin-orbital polarisation, such as to fill the $j_{\text{eff}}=3/2$ states entirely, leading to a half-filled $j_{\text{eff}}=1/2$ one-band picture, while in Sr_2RhO_4 the final situation is an effective two-orbital system containing three electrons. This situation is akin to correlation-induced enhancements of orbital polarisation also observed in other transition metal oxides. In the distorted $3d^1$ perovskites LaTiO_3 and YTiO_3 , for example, it was argued [10] that the interplay of structural distortions and Coulomb correlations leads to a suppression of orbital fluctuations in the t_{2g} -manifold, favoring a particular orbital composition selected by crystal and ligand field effects. At the LDA level, 0.45 [0.88] electrons are found in this particular orbital in LaTiO_3 [YTiO_3], while Coulomb correlations as described by LDA+DMFT lead to an occupation of 0.88 [0.96] electrons.

In these systems, this reduction of effective orbital degeneracy was shown to be key to their insulating nature since the critical interaction strength needed to localise the single electron is thus effectively determined by the one of a single-orbital system, instead of the one of a three-fold degenerate t_{2g} -manifold. Within DMFT, the critical Hubbard interaction scales with the square-root of the orbital degeneracy N for the lower critical interaction of the phase coexistence region of the first order Mott transition, while the upper critical interaction varies with N [231].

Localising electrons in a single-orbital system therefore needs a critical interaction roughly smaller by a factor of 3 as compared to the degenerate case. This was demonstrated to be crucial for the difference in behaviors in the series of d^1 compounds SrVO_3 , CaVO_3 , LaTiO_3 , YTiO_3 , where the former are three-fold degenerate metallic systems, whereas the latter realise the single-orbital Mott state.

The situation in the iridates is analogous with the purely formal difference that one is dealing with a one-hole situation instead of one electron. Furthermore, the strong spin-orbit interaction is instrumental for the suppression of the degeneracy, which is the net result of structural distortions, spin-orbit coupling and Coulomb correlations.

This discussion highlights an important aspect of the physics of transition metal oxides, often neglected when considering band filling and interaction strength only: the *effective orbital degeneracy* is a crucial tuning parameter for electronic behavior, suggesting that the popular

picture distinguishing filling-controlled and bandwidth-controlled Mott transitions [1] should be complemented by a “third axis” and the notion of degeneracy-controlled Mott behavior.

Crystal and ligand fields together with spin-orbit coupling and the Coulomb correlations themselves are the driving forces for establishing a given effective degeneracy. At the level of the calculations, this effective degeneracy is both an outcome of the calculation and a determining factor of the properties of the given compound.

6 Conclusions and Perspectives

The common belief about electronic Coulomb correlations being less important in 4d and 5d compounds as compared to 3d transition metal oxides, was overruled by insights into the role of spin-orbit coupling for the insulating behavior of iridates [16] and for the Fermi surface topology of Sr_2RhO_4 [19, 20].

Here, we have reviewed recent work on a first principles many-body description of such effects within a dynamical mean-field framework. We have highlighted the notion of the *effective degeneracy* of the system as a crucial parameter determining the physical properties of a system. The effective degeneracy is the result of a complex interplay of structural distortions spin-orbit coupling and Coulomb correlations. We have stressed the analogy of the $j_{\text{eff}}=1/2$ Mott insulating picture for Sr_2IrO_4 with the insulating nature of LaTiO_3 and YTiO_3 in the “degeneracy-controlled Mott transition” series of d^1 perovskites (SrVO_3 , CaVO_3 , LaTiO_3 , YTiO_3).

In Sr_2IrO_4 and Sr_2RhO_4 the difference in degeneracy is itself a consequence of the quantitative aspects of the physics of these two compounds: all three decisive elements – structural distortions, spin-orbit coupling and Hubbard interaction – are smaller in Sr_2RhO_4 than in Sr_2IrO_4 and this quantitative difference in the electronic parameters translates into a qualitative difference of the resulting properties.

We have analysed in detail the spectral properties of Sr_2RhO_4 , a spin-orbit correlated 4d metal where the effective degeneracy is reduced by spin-orbit coupling and correlations but not to the point such as to induce a $j_{\text{eff}}=1/2$ Mott insulator. The calculated spectral properties and Fermi surface are in excellent agreement with experimental data. A detailed analysis of the spectral properties of Sr_2IrO_4 is left for future work.

7 Acknowledgments

This work was supported by the ERC Consolidator Grant CORRELMAT (grant 617196), the French ANR under project IRIDATES, and IDRIS/GENCI under project t20169313. M.A. is supported by a START program of the Austrian Science Fund (FWF), grant number Y746.

Appendix A: Generalized partial Θ -projectors and spectral function

In order to calculate quantities for a given atom α and a particular orbital (spin) character j (m_j) – such as the spectral functions $A_j^{m_j\alpha}(\mathbf{k}, \omega)$ –, a set of partial projectors called “ Θ -projectors” was built. Contrary to the previously introduced Wannier projectors $P_{j,\nu}^{\alpha,m_j}(\mathbf{k})$, their definition is not restricted to the correlated orbitals only. The formalism of these partial projectors was initially introduced in [180] and was extended to the case where spin is not a good quantum number anymore in [21].

Inside the muffin-tin sphere associated to an atom α , one can write the spin- σ contribution of the eigenstate $\psi_{\mathbf{k}\nu}(\mathbf{r})$ as:

$$\phi_{\mathbf{k}\nu}^{\sigma}(\mathbf{r}) = \sum_{\ell=0}^{\ell_{max}} \sum_{m=-\ell}^{+\ell} \left[A_{\ell m}^{\nu\alpha}(\mathbf{k}, \sigma) u_{\ell m,1}^{\alpha,\sigma}(\mathbf{r}^{\alpha}) + B_{\ell m}^{\nu\alpha}(\mathbf{k}, \sigma) u_{\ell m,2}^{\alpha,\sigma}(\mathbf{r}^{\alpha}) + C_{\ell m}^{\nu\alpha}(\mathbf{k}, \sigma) u_{\ell m,3}^{\alpha,\sigma}(\mathbf{r}^{\alpha}) \right] \quad (24)$$

where the basis $\{u_{\ell m,i}^{\alpha,\sigma}\}_{i=\{1,2,3\}}$ is not orthonormalized as already mentioned in [180]. That is why, to make the calculations easier, one introduces an orthonormal basis set $\{v_{\ell m,j}^{\alpha,\sigma}\}_{j=\{1,2,3\}}$ for each atomic orbital (ℓ, m) . These orbitals are defined from the initial basis $\{u_{\ell m,i}^{\alpha,\sigma}\}_{i=\{1,2,3\}}$ as follows:

$$\forall i \quad u_{\ell m,i}^{\alpha,\sigma}(\mathbf{r}^{\alpha}) = \sum_{j=1}^3 c_{ij} v_{\ell m,j}^{\alpha,\sigma} \quad \text{with} \quad \mathbf{C} = \begin{pmatrix} 1 & 0 & \langle u_{\ell m,1}^{\alpha,\sigma} | u_{\ell m,2}^{\alpha,\sigma} \rangle \\ 0 & \langle u_{\ell m,2}^{\alpha,\sigma} | u_{\ell m,2}^{\alpha,\sigma} \rangle & \langle u_{\ell m,2}^{\alpha,\sigma} | u_{\ell m,3}^{\alpha,\sigma} \rangle \\ \langle u_{\ell m,3}^{\alpha,\sigma} | u_{\ell m,1}^{\alpha,\sigma} \rangle & \langle u_{\ell m,3}^{\alpha,\sigma} | u_{\ell m,2}^{\alpha,\sigma} \rangle & 1 \end{pmatrix}^{\frac{1}{2}}. \quad (25)$$

We can then rewrite (24) as:

$$\psi_{\mathbf{k}\nu}^{\sigma}(\mathbf{r}) = \sum_{\ell=0}^{\ell_{max}} \sum_{m=-\ell}^{+\ell} \sum_{i=1}^3 \Theta_{\ell m \nu, i}^{\alpha,\sigma}(\mathbf{k}) v_{\ell m, i}^{\alpha,\sigma}(\mathbf{r}^{\alpha}). \quad (26)$$

The matrix elements $\Theta_{\ell m \nu, i}^{\alpha,\sigma}(\mathbf{k})$ are the “ Θ -projectors”, which are thus defined by:

$$\Theta_{\ell m \nu, i}^{\alpha,\sigma}(\mathbf{k}) = \langle v_{\ell m, i}^{\alpha,\sigma} | \phi_{\mathbf{k}\nu}^{\sigma} \rangle = A_{\ell m}^{\nu\alpha}(\mathbf{k}, \sigma) c_{1i} + B_{\ell m}^{\nu\alpha}(\mathbf{k}, \sigma) c_{2i} + C_{\ell m}^{\nu\alpha}(\mathbf{k}, \sigma) c_{3i}. \quad (27)$$

Contrary to the implementation of [180], there is now a couple of Θ -projectors associated to each band index ν , $\Theta_{\ell m \nu, i}^{\alpha,\sigma}(\mathbf{k})$ with $\sigma = \uparrow, \downarrow$, since spin is not a good quantum number anymore.

We have introduced here the Θ -projectors in the complex spherical harmonics basis. As for the Wannier projectors, it is of course possible to get the Θ -projectors in any desired j, m_j basis:

$$\Theta_{j\nu, i}^{\alpha, m_j}(\mathbf{k}) = \sum_{m, \sigma} \mathcal{S}_{j, \ell m}^{m_j, \sigma} \Theta_{\ell m \nu, i}^{\alpha, \sigma}(\mathbf{k}) \quad (28)$$

Finally, the spectral function $A(\mathbf{k}, \omega)$ which is defined by:

$$A(\mathbf{k}, \omega) = -\frac{1}{\pi} \Im \mathfrak{m} [G(\mathbf{k}, \omega)]. \quad (29)$$

is obtained for a given atom α with orbital character (j, m_j) through the following formula:

$$A_j^{\alpha, m_j}(\mathbf{k}, \omega) = -\frac{1}{\pi} \Im \left[\sum_{\nu\nu'} \sum_{i=1}^3 \Theta_{j\nu, i}^{\alpha, m_j}(\mathbf{k}) \mathbf{G}_{\nu\nu'}(\mathbf{k}, \omega + i0^+) \left[\Theta_{j\nu', i}^{\alpha, m_j}(\mathbf{k}) \right]^* \right] \quad (30)$$

where the band indices ν, ν' run over *both* spin and orbital quantum number.

References

- [1] M. Imada, A. Fujimori, and Y. Tokura. Metal-insulator transitions. *Rev. Mod. Phys.*, 70(4):1039, Oct. 1998.
- [2] J. M. Tomczak, M. Casula, T. Miyake, and S. Biermann. Combined GW and dynamical mean-field theory: Dynamical screening effects in transition metal oxides. *EPL (Europhysics Letters)*, 100(6):67001, 2012.
- [3] J. M. Tomczak, M. Casula, T. Miyake, and S. Biermann. Asymmetry in band widening and quasiparticle lifetimes in SrVO₃: Competition between screened exchange and local correlations from combined *gw* and dynamical mean-field theory GW+DMFT. *Phys. Rev. B*, 90:165138, Oct 2014.
- [4] M. Aichhorn, S. Biermann, T. Miyake, A. Georges, and M. Imada. Theoretical evidence for strong correlations and incoherent metallic state in FeSe. *Phys. Rev. B*, 82:064504, Aug 2010.
- [5] A. van Roekeghem, T. Ayrat, J. M. Tomczak, M. Casula, N. Xu, H. Ding, M. Ferrero, O. Parcollet, H. Jiang, and S. Biermann. Dynamical correlations and screened exchange on the experimental bench: Spectral properties of the cobalt pnictide BaCo₂As₂. *Phys. Rev. Lett.*, 113:266403, Dec 2014.
- [6] A. van Roekeghem, P. Richard, X. Shi, S. Wu, L. Zeng, B. Scharf, Y. Ohtsubo, T. Qian, A. S. Sefat, S. Biermann, and H. Ding. Tetragonal and collapsed-tetragonal phases of CaFe₂As₂: A view from angle-resolved photoemission and dynamical mean-field theory. *Phys. Rev. B*, 93:245139, Jun 2016.
- [7] E. Razzoli, C. E. Matt, M. Kobayashi, X.-P. Wang, V. N. Strocov, A. van Roekeghem, S. Biermann, N. C. Plumb, M. Radovic, T. Schmitt, C. Capan, Z. Fisk, P. Richard, H. Ding, P. Aebi, J. Mesot, and M. Shi. Tuning electronic correlations in transition metal pnictides: Chemistry beyond the valence count. *Phys. Rev. B*, 91:214502, Jun 2015.
- [8] J.-Z. Ma, A. van Roekeghem, P. Richard, Z.-H. Liu, H. Miao, L.-K. Zeng, N. Xu, M. Shi, C. Cao, J.-B. He, G.-F. Chen, Y.-L. Sun, G.-H. Cao, S.-C. Wang, S. Biermann, T. Qian, and H. Ding. Correlation-induced self-doping in the iron-pnictide superconductor Ba₂Ti₂Fe₂As₄O. *Phys. Rev. Lett.*, 113:266407, Dec 2014.
- [9] K Haule and G Kotliar. Coherence-incoherence crossover in the normal state of iron oxypnictides and importance of Hund’s rule coupling. *New Journal of Physics*, 11(2):025021, 2009.

- [10] E. Pavarini, S. Biermann, A. Poteryaev, A. I. Lichtenstein, A. Georges, and O. K. Andersen. Mott Transition and Suppression of Orbital Fluctuations in Orthorhombic $3d^1$ Perovskites. *Phys. Rev. Lett.*, 92(17):176403, Apr. 2004.
- [11] A. I. Poteryaev, J. M. Tomczak, S. Biermann, A. Georges, A. I. Lichtenstein, A. N. Rubtsov, T. Saha-Dasgupta, and O. K. Andersen. Enhanced crystal-field splitting and orbital-selective coherence induced by strong correlations in V_2O_3 . *Phys. Rev. B*, 76:085127, Aug 2007.
- [12] J. M. Tomczak, A. I. Poteryaev, and S. Biermann. Momentum-resolved spectroscopy of correlated metals: A view from dynamical mean field theory. *Comptes Rendus Physique*, 10(6):537 – 547, 2009.
- [13] G. Keller, K. Held, V. Eyert, D. Vollhardt, and V. I. Anisimov. Electronic structure of paramagnetic v_2o_3 : Strongly correlated metallic and Mott insulating phase. *Phys. Rev. B*, 70(20):205116, 2004.
- [14] K. Held, G. Keller, V. Eyert, D. Vollhardt, and V. I. Anisimov. Mott-Hubbard metal-insulator transition in paramagnetic V_2O_3 : An LDA+DMFT(QMC) study. *Phys. Rev. Lett.*, 86(23):5345–5348, Jun 2001.
- [15] B. J. Kim, H. Ohsumi, T. Komesu, S. Sakai, T. Morita, H. Takagi, and T. Arima. Phase-Sensitive Observation of a Spin-Orbital Mott State in Sr_2IrO_4 . *Science*, 323(5919):1329, Mar. 2009.
- [16] B. J. Kim, H. Jin, S. J. Moon, J.-Y. Kim, B.-G. Park, C. S. Leem, Jaejun Yu, T. W. Noh, C. Kim, S.-J. Oh, J.-H. Park, V. Durairaj, G. Cao, and E. Rotenberg. Novel $J_{\text{eff}} = 1/2$ Mott state induced by relativistic spin-orbit coupling in Sr_2IrO_4 . *Phys. Rev. Lett.*, 101:076402, Aug 2008.
- [17] J. G. Rau, E. K.-H. Lee, and H.-Y. Kee. Spin-orbit physics giving rise to novel phases in correlated systems: Iridates and related materials. *Annual Review of Condensed Matter Physics*, 7:195–221, 2016.
- [18] W. Witczak-Krempa, G. Chen, Y. B. Kim, and L. Balents. Correlated quantum phenomena in the strong spin-orbit regime. *Annual Review of Condensed Matter Physics*, 5:57–82, 2014.
- [19] M. W. Haverkort, I. S. Elfimov, L. H. Tjeng, G. A. Sawatzky, and A. Damascelli. Strong Spin-Orbit Coupling Effects on the Fermi Surface of Sr_2RuO_4 and Sr_2RhO_4 . *Phys. Rev. Lett.*, 101(2):026406, Jul. 2008.
- [20] G.-Q. Liu, V. N. Antonov, O. Jepsen, and O. K. Andersen. Coulomb-Enhanced Spin-Orbit Splitting: The Missing Piece in the Sr_2RhO_4 Puzzle. *Phys. Rev. Lett.*, 101(2):026408, Jul. 2008.
- [21] C. Martins, M. Aichhorn, L. Vaugier, and S. Biermann. Reduced effective spin-orbital degeneracy and spin-orbital ordering in paramagnetic transition-metal oxides: Sr_2IrO_4 versus Sr_2RhO_4 . *Phys. Rev. Lett.*, 107:266404, Dec 2011.

- [22] K.-H. Ahn, K.-W. Lee, and J. Kuneš. Doping-dependent bandwidth renormalization and spinorbit coupling in $(\text{Sr}_{1-x}\text{La}_x)_2\text{RhO}_4$. *Journal of Physics: Condensed Matter*, 27(8):085602, 2015.
- [23] Y. Ando. Topological insulator materials. *J. Phys. Soc. Jpn.*, 82:102001, 2013.
- [24] M. Z. Hasan and C. L. Kane. *Colloquium* : Topological insulators. *Rev. Mod. Phys.*, 82:3045–3067, Nov 2010.
- [25] X.-L. Qi and S.-C. Zhang. Topological insulators and superconductors. *Rev. Mod. Phys.*, 83:1057–1110, Oct 2011.
- [26] L. Perfetti, P. A. Loukakos, M. Lisowski, U. Bovensiepen, H. Berger, S. Biermann, P. S. Cornaglia, A. Georges, and M. Wolf. Time evolution of the electronic structure of 1T-TaS₂ through the insulator-metal transition. *Phys. Rev. Lett.*, 97:067402, Aug 2006.
- [27] T. Ritschel, J. Trinckauf, K. Koepernik, B. Büchner, M. v. Zimmermann, H. Berger, Y.I. Joe, P. Abbamonte, and J. Geck. Orbital textures and charge density waves in transition metal dichalcogenides. *Nat. Phys.*, 11:328, 2015.
- [28] L. Ma, C. Ye, Y. Yu, X. F. Lu, X. Niu, S. Kim, D. Feng, D. Tomanek, Y.-W. Son, X. H. Chen, and Y. Zhang. A metallic mosaic phase and the origin of Mott-insulating state in 1T-TaS₂. *Nat. Comm.*, 7:10956, 2016.
- [29] L. Perfetti, A. Georges, S. Florens, S. Biermann, S. Mitrovic, H. Berger, Y. Tamm, H. Höchst, and M. Grioni. Spectroscopic signatures of a bandwidth-controlled Mott transition at the surface of 1T-TaSe₂. *Phys. Rev. Lett.*, 90:166401, Apr 2003.
- [30] Y. Shi, Y. Guo, X. Wang, A. J. Princep, D. Khalyavin, P. Manuel, Y. Michiue, A. Sato, K. Tsuda, S. Yu, M. Arai, Y. Shirako, M. Akaogi, N. Wang, K. Yamaura, and A. T. Boothroyd. A ferroelectric-like structural transition in a metal. *Nature Materials*, 12:1024, Jun 2013.
- [31] Y. G. Shi, Y. F. Guo, S. Yu, M. Arai, A. A. Belik, A. Sato, K. Yamaura, E. Takayama-Muromachi, H. F. Tian, H. X. Yang, J. Q. Li, T. Varga, J. F. Mitchell, and S. Okamoto. Continuous metal-insulator transition of the antiferromagnetic perovskite NaOsO₃. *Phys. Rev. B*, 80:161104, Oct 2009.
- [32] M.-C. Jung, Y.-J. Song, K.-W. Lee, and W. E. Pickett. Structural and correlation effects in the itinerant insulating antiferromagnetic perovskite NaOsO₃. *Phys. Rev. B*, 87:115119, Mar 2013.
- [33] S. Calder, V. O. Garlea, D. F. McMorrow, M. D. Lumsden, M. B. Stone, J. C. Lang, J.-W. Kim, J. A. Schlueter, Y. G. Shi, K. Yamaura, Y. S. Sun, Y. Tsujimoto, and A. D. Christianson. Magnetically driven metal-insulator transition in NaOsO₃. *Phys. Rev. Lett.*, 108:257209, Jun 2012.
- [34] Y. Du, X. Wan, L. Sheng, J. Dong, and S. Y. Savrasov. Electronic structure and magnetic properties of NaOsO₃. *Phys. Rev. B*, 85:174424, May 2012.

- [35] I. Lo Vecchio, A. Perucchi, P. Di Pietro, O. Limaj, U. Schade, Y. Sun, M. Arai, K. Yamaura, and S. Lupi. Infrared evidence of a Slater metal-insulator transition in NaOsO_3 . *Scientific Reports*, 3:2990, Oct 2013.
- [36] S. Calder, J. H. Lee, M. B. Stone, M. D. Lumsden, J. C. Lang, M. Feygenson, Z. Zhao, J.-Q. Yan, Y. G. Shi, Y. S. Sun, Y. Tsujimoto, K. Yamaura, and A. D. Christianson. Enhanced spin-phonon-electronic coupling in a $5d$ oxide. *Nature Communications*, 6:8916, Nov 2015.
- [37] G. Khaliullin. Excitonic magnetism in Van Vleck-type d^4 Mott insulators. *Phys. Rev. Lett.*, 111:197201, Nov 2013.
- [38] A. Subedi. First-principles study of the electronic structure and magnetism of CaIrO_3 . *Phys. Rev. B*, 85:020408, Jan 2012.
- [39] M. Moretti Sala, K. Ohgushi, A. Al-Zein, Y. Hirata, G. Monaco, and M. Krisch. CaIrO_3 : A spin-orbit Mott insulator beyond the $J_{\text{eff}} = 1/2$ ground state. *Phys. Rev. Lett.*, 112:176402, Apr 2014.
- [40] Sun-Woo Kim, Chen Liu, Hyun-Jung Kim, Jun-Ho Lee, Yongxin Yao, Kai-Ming Ho, and Jun-Hyung Cho. Nature of the insulating ground state of the $5d$ postperovskite CaIrO_3 . *Phys. Rev. Lett.*, 115:096401, Aug 2015.
- [41] M. Bremholm, S.E. Dutton, P.W. Stephens, and R.J. Cava. NaIrO_3 – A pentavalent post-perovskite. *Journal of Solid State Chemistry*, 184(3):601 – 607, 2011.
- [42] L. Du, X. Sheng, H. Weng, and X. Dai. The electronic structure of NaIrO_3 , Mott insulator or band insulator? *EPL (Europhysics Letters)*, 101(2):27003, 2013.
- [43] K. Maiti, Ra. S. Singh, V. R. R. Medicherla, S. Rayaprol, and E. V. Sampathkumaran. Origin of charge density wave formation in insulators from a high resolution photoemission study of BaIrO_3 . *Phys. Rev. Lett.*, 95:016404, Jun 2005.
- [44] J.-G. Cheng, J.-S. Zhou, J. A. Alonso, J. B. Goodenough, Y. Sui, K. Matsubayashi, and Y. Uwatoko. Transition from a weak ferromagnetic insulator to an exchange-enhanced paramagnetic metal in the BaIrO_3 polytypes. *Phys. Rev. B*, 80:104430, Sep 2009.
- [45] W. Ju, G.-Q. Liu, and Z. Yang. Exotic spin-orbital Mott insulating states in BaIrO_3 . *Phys. Rev. B*, 87:075112, Feb 2013.
- [46] S. J. Moon, H. Jin, K. W. Kim, W. S. Choi, Y. S. Lee, J. Yu, G. Cao, A. Sumi, H. Funakubo, C. Bernhard, and T. W. Noh. Dimensionality-Controlled Insulator-Metal Transition and Correlated Metallic State in $5d$ Transition Metal Oxides $\text{Sr}_{n+1}\text{Ir}_n\text{O}_{3n+1}$ ($n = 1, 2$, and ∞). *Phys. Rev. Lett.*, 101(22):226402, Nov. 2008.
- [47] G. Cao, V. Durairaj, S. Chikara, L. E. DeLong, S. Parkin, and P. Schlottmann. Non-Fermi-liquid behavior in nearly ferromagnetic SrIrO_3 single crystals. *Phys. Rev. B*, 76:100402, Sep 2007.

- [48] Y. F. Nie, P. D. C. King, C. H. Kim, M. Uchida, H. I. Wei, B. D. Faeth, J. P. Ruf, J. P. C. Ruff, L. Xie, X. Pan, C. J. Fennie, D. G. Schlom, and K. M. Shen. Interplay of spin-orbit interactions, dimensionality, and octahedral rotations in semimetallic SrIrO_3 . *Phys. Rev. Lett.*, 114:016401, Jan 2015.
- [49] S. J. Moon. Temperature dependence of the optical response of perovskite-type SrIrO_3 thin film. *Journal of the Korean Physical Society*, 64(8):1174–1178, 2014.
- [50] Y. Singh and P. Gegenwart. Antiferromagnetic Mott insulating state in single crystals of the honeycomb lattice material Na_2IrO_3 . *Phys. Rev. B*, 82:064412, Aug 2010.
- [51] R. Comin, G. Levy, B. Ludbrook, Z.-H. Zhu, C. N. Veenstra, J. A. Rosen, Y. Singh, P. Gegenwart, D. Stricker, J. N. Hancock, D. van der Marel, I. S. Elfimov, and A. Damascelli. Na_2IrO_3 as a novel relativistic Mott insulator with a 340 meV gap. *Phys. Rev. Lett.*, 109:266406, Dec 2012.
- [52] X. Liu, T. Berlijn, W.-G. Yin, W. Ku, A. Tsvelik, Y.-J. Kim, H. Gretarsson, Y. Singh, P. Gegenwart, and J. P. Hill. Long-range magnetic ordering in Na_2IrO_3 . *Phys. Rev. B*, 83:220403, Jun 2011.
- [53] H. Gretarsson, J. P. Clancy, X. Liu, J. P. Hill, Emil Bozin, Yogesh Singh, S. Manni, P. Gegenwart, Jungho Kim, A. H. Said, D. Casa, T. Gog, M. H. Upton, Heung-Sik Kim, J. Yu, Vamshi M. Katukuri, L. Hozoi, Jeroen van den Brink, and Young-June Kim. Crystal-field splitting and correlation effect on the electronic structure of A_2IrO_3 . *Phys. Rev. Lett.*, 110:076402, Feb 2013.
- [54] J. Chaloupka and G. Khaliullin. Hidden symmetries of the extended Kitaev-Heisenberg model: Implications for the honeycomb-lattice iridates A_2IrO_3 . *Phys. Rev. B*, 92:024413, Jul 2015.
- [55] J. Chaloupka and G. Khaliullin. Magnetic anisotropy in the Kitaev model systems Na_2IrO_3 and RuCl_3 . *Phys. Rev. B*, 94:064435, Aug 2016.
- [56] Y. Singh, S. Manni, J. Reuther, T. Berlijn, R. Thomale, W. Ku, S. Trebst, and P. Gegenwart. Relevance of the Heisenberg-Kitaev model for the honeycomb lattice iridates A_2IrO_3 . *Phys. Rev. Lett.*, 108:127203, Mar 2012.
- [57] J. Reuther, R. Thomale, and S. Rachel. Spiral order in the honeycomb iridate Li_2IrO_3 . *Phys. Rev. B*, 90:100405, Sep 2014.
- [58] A. Biffin, R. D. Johnson, Sungkyun Choi, F. Freund, S. Manni, A. Bombardi, P. Manuel, P. Gegenwart, and R. Coldea. Unconventional magnetic order on the hyperhoneycomb Kitaev lattice in $\beta\text{-Li}_2\text{IrO}_3$: Full solution via magnetic resonant x-ray diffraction. *Phys. Rev. B*, 90:205116, Nov 2014.
- [59] T. Takayama, A. Kato, R. Dinnebier, J. Nuss, H. Kono, L. S. I. Veiga, G. Fabbri, D. Haskel, and H. Takagi. Hyperhoneycomb iridate $\beta\text{-Li}_2\text{IrO}_3$ as a platform for Kitaev magnetism. *Phys. Rev. Lett.*, 114:077202, Feb 2015.

- [60] A. Biffin, R. D. Johnson, I. Kimchi, R. Morris, A. Bombardi, J. G. Analytis, A. Vishwanath, and R. Coldea. Noncoplanar and counterrotating incommensurate magnetic order stabilized by Kitaev interactions in γ -Li₂IrO₃. *Phys. Rev. Lett.*, 113:197201, Nov 2014.
- [61] H. Okabe, N. Takeshita, M. Isobe, E. Takayama-Muromachi, T. Muranaka, and J. Akimitsu. Pressure-induced metal-insulator transition in the spin-orbit Mott insulator Ba₂IrO₄. *Phys. Rev. B*, 84:115127, Sep 2011.
- [62] R. Arita, J. Kuneš, A. V. Kozhevnikov, A. G. Eguiluz, and M. Imada. *Ab initio* studies on the interplay between spin-orbit interaction and Coulomb correlation in Sr₂IrO₄ and Ba₂IrO₄. *Phys. Rev. Lett.*, 108:086403, Feb 2012.
- [63] Vamshi M. Katukuri, Hermann Stoll, Jeroen van den Brink, and Liviu Hozoi. *Ab initio* determination of excitation energies and magnetic couplings in correlated quasi-two-dimensional iridates. *Phys. Rev. B*, 85:220402, Jun 2012.
- [64] S. Moser, L. Moreschini, A. Ebrahimi, B. Dalla Piazza, M. Isobe, H. Okabe, J. Akimitsu, V. V. Mazurenko, K. S. Kim, A. Bostwick, E. Rotenberg, J. Chang, H. M. Ronnow, and M. Grioni. The electronic structure of the high-symmetry perovskite iridate Ba₂IrO₄. *New Journal of Physics*, 16(1):013008, 2014.
- [65] S. Calder, G.-X. Cao, S. Okamoto, J. W. Kim, V. R. Cooper, Z. Gai, B. C. Sales, M. D. Lumsden, D. Mandrus, and A. D. Christianson. $J_{\text{eff}} = \frac{1}{2}$ Mott spin-orbit insulating state close to the cubic limit in Ca₄IrO₆. *Phys. Rev. B*, 89:081104, Feb 2014.
- [66] G. Cao, V. Durairaj, S. Chikara, S. Parkin, and P. Schlottmann. Partial antiferromagnetism in spin-chain Sr₅Rh₄O₁₂, Ca₅Ir₃O₁₂, and Ca₄IrO₆ single crystals. *Phys. Rev. B*, 75:134402, Apr 2007.
- [67] I. Franke, P. J. Baker, S. J. Blundell, T. Lancaster, W. Hayes, F. L. Pratt, and G. Cao. Measurement of the internal magnetic field in the correlated iridates Ca₄IrO₆, Ca₅Ir₃O₁₂, Sr₃Ir₂O₇ and Sr₂IrO₄. *Phys. Rev. B*, 83:094416, Mar 2011.
- [68] M. C. Shapiro, Scott C. Riggs, M. B. Stone, C. R. de la Cruz, S. Chi, A. A. Podlesnyak, and I. R. Fisher. Structure and magnetic properties of the pyrochlore iridate Y₂Ir₂O₇. *Phys. Rev. B*, 85:214434, Jun 2012.
- [69] Steven M. Disseler. Direct evidence for the all-in/all-out magnetic structure in the pyrochlore iridates from muon spin relaxation. *Phys. Rev. B*, 89:140413, Apr 2014.
- [70] Kazuyuki Matsuhira, Makoto Wakeshima, Yukio Hinatsu, and Seishi Takagi. Metalinsulator transitions in pyrochlore oxides Ln₂Ir₂O₇. *Journal of the Physical Society of Japan*, 80(9):094701, 2011.
- [71] T. Kondo, M. Nakayama, R. Chen, J. J. Ishikawa, E.-G. Moon, T. Yamamoto, Y. Ota, W. Malaeb, H. Kanai, Y. Nakashima, Y. Ishida, R. Yoshida, H. Yamamoto, M. Matsunami, S. Kimura, N. Inami, K. Ono, H. Kumigashira, S. Nakatsuji, L. Balents, and S. Shin. Quadratic Fermi node in a 3D strongly correlated semimetal. *Nat. Commun.*, 6:10042, Dec 2015.

- [72] Kazuyuki Matsuhira, Makoto Wakeshima, Ryo Nakanishi, Takaaki Yamada, Akira Nakamura, Wataru Kawano, Seishi Takagi, and Yukio Hinatsu. Metal-insulator transition in pyrochlore iridates $\text{Ln}_2\text{Ir}_2\text{O}_7$ ($\text{Ln} = \text{Nd}, \text{Sm}, \text{and Eu}$). *Journal of the Physical Society of Japan*, 76(4):043706, 2007.
- [73] H. Sagayama, D. Uematsu, T. Arima, K. Sugimoto, J. J. Ishikawa, E. O’Farrell, and S. Nakatsuji. Determination of long-range all-in/all-out ordering of Ir^{4+} moments in a pyrochlore iridate $\text{Eu}_2\text{Ir}_2\text{O}_7$ by resonant X-ray diffraction. *Phys. Rev. B*, 87:100403, Mar 2013.
- [74] A. B. Sushkov, J. B. Hofmann, G. S. Jenkins, J. Ishikawa, S. Nakatsuji, S. Das Sarma, and H. D. Drew. Optical evidence for a weyl semimetal state in pyrochlore $\text{Eu}_2\text{Ir}_2\text{O}_7$. *Phys. Rev. B*, 92:241108, Dec 2015.
- [75] D. Uematsu, H. Sagayama, T. Arima, J. J. Ishikawa, S. Nakatsuji, H. Takagi, M. Yoshida, J. Mizuki, and K. Ishii. Large trigonal-field effect on spin-orbit coupled states in a pyrochlore iridate. *Phys. Rev. B*, 92:094405, Sep 2015.
- [76] E. Lefrançois, V. Simonet, R. Ballou, E. Lhotel, A. Hadj-Azzem, S. Kodjikian, P. Lejay, P. Manuel, D. Khalyavin, and L. C. Chapon. Anisotropy-tuned magnetic order in pyrochlore iridates. *Phys. Rev. Lett.*, 114:247202, Jun 2015.
- [77] S. M. Disseler, Chetan Dhital, A. Amato, S. R. Giblin, Clarina de la Cruz, Stephen D. Wilson, and M. J. Graf. Magnetic order in the pyrochlore iridates $\text{A}_2\text{Ir}_2\text{O}_7$ ($\text{A} = \text{Y}, \text{Yb}$). *Phys. Rev. B*, 86:014428, Jul 2012.
- [78] Nobuyuki Taira, Makoto Wakeshima, and Yukio Hinatsu. Magnetic properties of iridium pyrochlores $\text{R}_2\text{Ir}_2\text{O}_7$ ($\text{R} = \text{Y}, \text{Sm}, \text{Eu and Lu}$). *Journal of Physics: Condensed Matter*, 13(23):5527, 2001.
- [79] Y. S. Lee, S. J. Moon, Scott C. Riggs, M. C. Shapiro, I. R. Fisher, Bradford W. Fulfer, Julia Y. Chan, A. F. Kemper, and D. N. Basov. Infrared study of the electronic structure of the metallic pyrochlore iridate $\text{Bi}_2\text{Ir}_2\text{O}_7$. *Phys. Rev. B*, 87:195143, May 2013.
- [80] T. F. Qi, O. B. Korneta, Xiangang Wan, L. E. DeLong, P. Schlottmann, and G. Cao. Strong magnetic instability in correlated metallic $\text{Bi}_2\text{Ir}_2\text{O}_7$. *Journal of Physics: Condensed Matter*, 24(34):345601, 2012.
- [81] G. Cao, Y. Xin, C. S. Alexander, J. E. Crow, P. Schlottmann, M. K. Crawford, R. L. Harlow, and W. Marshall. Anomalous magnetic and transport behavior in the magnetic insulator $\text{Sr}_3\text{Ir}_2\text{O}_7$. *Phys. Rev. B*, 66:214412, Dec 2002.
- [82] S. Fujiyama, K. Ohashi, H. Ohsumi, K. Sugimoto, T. Takayama, T. Komesu, M. Takata, T. Arima, and H. Takagi. Weak antiferromagnetism of $J_{\text{eff}} = \frac{1}{2}$ band in bilayer iridate $\text{Sr}_3\text{Ir}_2\text{O}_7$. *Phys. Rev. B*, 86:174414, Nov 2012.
- [83] H. J. Park, C. H. Sohn, D. W. Jeong, G. Cao, K. W. Kim, S. J. Moon, H. Jin, D.-Y. Cho, and T. W. Noh. Phonon-assisted optical excitation in the narrow bandgap Mott insulator $\text{Sr}_3\text{Ir}_2\text{O}_7$. *Phys. Rev. B*, 89:155115, Apr 2014.

- [84] T. Hogan, L. Bjaalie, L. Zhao, C. Belvin, X. Wang, C. G. Van de Walle, D. Hsieh, and S. D. Wilson. Structural investigation of the bilayer iridate $\text{Sr}_3\text{Ir}_2\text{O}_7$. *Phys. Rev. B*, 93:134110, Apr 2016.
- [85] Junggho Kim, A. H. Said, D. Casa, M. H. Upton, T. Gog, M. Daghofer, G. Jackeli, J. van den Brink, G. Khaliullin, and B. J. Kim. Large spin-wave energy gap in the bilayer iridate $\text{Sr}_3\text{Ir}_2\text{O}_7$: Evidence for enhanced dipolar interactions near the Mott metal-insulator transition. *Phys. Rev. Lett.*, 109:157402, Oct 2012.
- [86] Yoshihiko Okamoto, Minoru Nohara, Hiroko Aruga-Katori, and Hidenori Takagi. Spin-liquid state in the $S = 1/2$ hyperkagome antiferromagnet $\text{Na}_4\text{Ir}_3\text{O}_8$. *Phys. Rev. Lett.*, 99:137207, Sep 2007.
- [87] Rebecca Dally, Tom Hogan, Alex Amato, Hubertus Luetkens, Chris Baines, Jose Rodriguez-Rivera, Michael J. Graf, and Stephen D. Wilson. Short-range correlations in the magnetic ground state of $\text{Na}_4\text{Ir}_3\text{O}_8$. *Phys. Rev. Lett.*, 113:247601, Dec 2014.
- [88] Ashiwini Balodhi, A. Thamizhavel, and Yogesh Singh. Evolution of magnetic, transport, and thermal properties in $\text{Na}_{4-x}\text{Ir}_3\text{O}_8$. *Phys. Rev. B*, 91:224409, Jun 2015.
- [89] Makoto Wakeshima, Nobuyuki Taira, Yukio Hinatsu, and Yoshinobu Ishii. Electrical and magnetic properties of pseudo-one-dimensional calcium iridium oxide $\text{Ca}_5\text{Ir}_3\text{O}_{12}$. *Solid State Communications*, 125(6):311 – 315, 2003.
- [90] G. Cao, A. Subedi, S. Calder, J.-Q. Yan, J. Yi, Z. Gai, L. Poudel, D. J. Singh, M. D. Lumsden, A. D. Christianson, Brian C. Sales, and D. Mandrus. Magnetism and electronic structure of $\text{La}_2\text{ZnIrO}_6$ and $\text{La}_2\text{MgIrO}_6$: Candidate $J_{\text{eff}} = \frac{1}{2}$ Mott insulators. *Phys. Rev. B*, 87:155136, Apr 2013.
- [91] M. P. Ghimire, L.-H. Wu, and X. Hu. Possible half-metallic antiferromagnetism in an iridium double-perovskite material. *Phys. Rev. B*, 93:134421, Apr 2016.
- [92] S. J. Mugavero III, A. H. Fox, M. D. Smith, and H.-C. zur Loye. Crystal growth, structure and magnetic properties of the double perovskites $\text{Ln}_2\text{MgIrO}_6$ ($\text{Ln}=\text{Pr}, \text{Nd}, \text{SmGd}$). *Journal of Solid State Chemistry*, 183(2):465 – 470, 2010.
- [93] Daijitsu Harada, Makoto Wakeshima, and Yukio Hinatsu. The structure and magnetic properties of new iridium (IV) perovskites $\text{Sr}_2\text{LnIrO}_6$ ($\text{Ln}=\text{Ce}, \text{Tb}$). *Journal of Solid State Chemistry*, 145(1):356 – 360, 1999.
- [94] S. K. Panda and I. Dasgupta. Electronic structure and magnetism in Ir-based double-perovskite $\text{Sr}_2\text{CeIrO}_6$. *Modern Physics Letters B*, 27(06):1350041, 2013.
- [95] S. Kanungo, K. Mogare, B. Yan, C. Felser, and M. Jansen. Orbital ordering of Ir- t_{2g} states in the double perovskite $\text{Sr}_2\text{CeIrO}_6$. *arXiv:cond-mat/1507.08682 (unpublished)*, 2015.
- [96] T. Dey, A. Maljuk, D. V. Efremov, O. Kataeva, S. Gass, C. G. F. Blum, F. Steckel, D. Gruner, T. Ritschel, A. U. B. Wolter, J. Geck, C. Hess, K. Koepernik, J. van den Brink, S. Wurmehl, and B. Büchner. Ba_2YIrO_6 : A cubic double perovskite material with Ir^{5+} ions. *Phys. Rev. B*, 93:014434, Jan 2016.

- [97] Tusharkanti Dey, A. V. Mahajan, P. Khuntia, M. Baenitz, B. Koteswararao, and F. C. Chou. Spin-liquid behavior in $J_{\text{eff}} = \frac{1}{2}$ triangular lattice compound $\text{Ba}_3\text{IrTi}_2\text{O}_9$. *Phys. Rev. B*, 86:140405, Oct 2012.
- [98] Andrei Catuneanu, Jeffrey G. Rau, Heung-Sik Kim, and Hae-Young Kee. Magnetic orders proximal to the Kitaev limit in frustrated triangular systems: Application to $\text{Ba}_3\text{IrTi}_2\text{O}_9$. *Phys. Rev. B*, 92:165108, Oct 2015.
- [99] Tusharkanti Dey, R. Kumar, A. V. Mahajan, S. D. Kaushik, and V. Siruguri. Unconventional magnetism in the spin-orbit-driven Mott insulators $\text{Ba}_3\text{M}\text{Ir}_2\text{O}_9$ ($M = \text{Sc}, \text{Y}$). *Phys. Rev. B*, 89:205101, May 2014.
- [100] Abhishek Nag, S. Middey, Sayantika Bhowal, S. K. Panda, Roland Mathieu, J. C. Orain, F. Bert, P. Mendels, P. G. Freeman, M. Mansson, H. M. Ronnow, M. Telling, P. K. Biswas, D. Sheptyakov, S. D. Kaushik, Vasudeva Siruguri, Carlo Meneghini, D. D. Sarma, Indra Dasgupta, and Sugata Ray. Origin of the spin-orbital liquid state in a nearly $j = 0$ iridate $\text{Ba}_3\text{ZnIr}_2\text{O}_9$. *Phys. Rev. Lett.*, 116:097205, Mar 2016.
- [101] J.-S. Zhou, K. Matsubayashi, Y. Uwatoko, C.-Q. Jin, J.-G. Cheng, J. B. Goodenough, Q. Q. Liu, T. Katsura, A. Shatskiy, and E. Ito. Critical behavior of the ferromagnetic perovskite BaRuO_3 . *Phys. Rev. Lett.*, 101:077206, Aug 2008.
- [102] C.-Q. Jin, J.-S. Zhou, J. B. Goodenough, Q. Q. Liu, J. G. Zhao, L. X. Yang, Y. Yu, R. C. Yu, T. Katsura, A. Shatskiy, and E. Ito. High-pressure synthesis of the cubic perovskite BaRuO_3 and evolution of ferromagnetism in ARuO_3 ($A = \text{Ca}, \text{Sr}, \text{Ba}$) ruthenates. *Proceedings of the National Academy of Sciences*, 105(20):7115–7119, 2008.
- [103] Qiang Han, Hung T. Dang, and A. J. Millis. Ferromagnetism and correlation strength in cubic barium ruthenate in comparison to strontium and calcium ruthenate: A dynamical mean-field study. *Phys. Rev. B*, 93:155103, Apr 2016.
- [104] J. M. Longo, P. M. Raccach, and J. B. Goodenough. Magnetic properties of SrRuO_3 and CaRuO_3 . *Journal of Applied Physics*, 39(2):1327–1328, 1968.
- [105] M. Schneider, D. Geiger, S. Esser, U. S. Pracht, C. Stingl, Y. Tokiwa, V. Moshnyaga, I. Sheikin, J. Mravlje, M. Scheffler, and P. Gegenwart. Low-energy electronic properties of clean CaRuO_3 : Elusive Landau quasiparticles. *Phys. Rev. Lett.*, 112:206403, May 2014.
- [106] L. Capogna, A. P. Mackenzie, R. S. Perry, S. A. Grigera, L. M. Galvin, P. Raychaudhuri, A. J. Schofield, C. S. Alexander, G. Cao, S. R. Julian, and Y. Maeno. Sensitivity to disorder of the metallic state in the ruthenates. *Phys. Rev. Lett.*, 88:076602, Feb 2002.
- [107] Yoshihiko Noro and Syôhei Miyahara. Electrical resistivity of SrRuO_3 . *Journal of the Physical Society of Japan*, 27(2):518A–518A, 1969.
- [108] C. G. Fatuzzo, M. Dantz, S. Fatale, P. Olalde-Velasco, N. E. Shaik, B. Dalla Piazza, S. Toth, J. Pelliciari, R. Fittipaldi, A. Vecchione, N. Kikugawa, J. S. Brooks, H. M. Ronnow, M. Grioni, Ch. Rüegg, T. Schmitt, and J. Chang. Spin-orbit-induced orbital

excitations in Sr_2RuO_4 and Ca_2RuO_4 : A resonant inelastic X-ray scattering study. *Phys. Rev. B*, 91:155104, Apr 2015.

- [109] Guoren Zhang, Evgeny Gorelov, Esmaeel Sarvestani, and Eva Pavarini. Fermi surface of Sr_2RuO_4 : Spin-orbit and anisotropic Coulomb interaction effects. *Phys. Rev. Lett.*, 116:106402, Mar 2016.
- [110] C. S. Alexander, G. Cao, V. Dobrosavljevic, S. McCall, J. E. Crow, E. Lochner, and R. P. Guertin. Destruction of the Mott insulating ground state of Ca_2RuO_4 by a structural transition. *Phys. Rev. B*, 60:R8422–R8425, Sep 1999.
- [111] T. Mizokawa, L. H. Tjeng, G. A. Sawatzky, G. Ghiringhelli, O. Tjernberg, N. B. Brookes, H. Fukazawa, S. Nakatsuji, and Y. Maeno. Spin-orbit coupling in the Mott insulator Ca_2RuO_4 . *Phys. Rev. Lett.*, 87:077202, Jul 2001.
- [112] Guo-Qiang Liu. Competition between spin-orbit coupling and magnetic exchange splitting in Ca_2RuO_4 . *Phys. Rev. B*, 88:104428, Sep 2013.
- [113] W. Tian, C. Svoboda, M. Ochi, M. Matsuda, H. B. Cao, J.-G. Cheng, B. C. Sales, D. G. Mandrus, R. Arita, N. Trivedi, and J.-Q. Yan. High antiferromagnetic transition temperature of the honeycomb compound SrRu_2O_6 . *Phys. Rev. B*, 92:100404, Sep 2015.
- [114] C. I. Hiley, D. O. Scanlon, A. A. Sokol, S. M. Woodley, A. M. Ganose, S. Sangiao, J. M. De Teresa, P. Manuel, D. D. Khalyavin, M. Walker, M. R. Lees, and R. I. Walton. Antiferromagnetism at $T > 500\text{ K}$ in the layered hexagonal ruthenate SrRu_2O_6 . *Phys. Rev. B*, 92:104413, Sep 2015.
- [115] A. Tamai, M. P. Allan, J. F. Mercure, W. Meevasana, R. Dunkel, D. H. Lu, R. S. Perry, A. P. Mackenzie, D. J. Singh, Z.-X. Shen, and F. Baumberger. Fermi surface and van Hove singularities in the itinerant metamagnet $\text{Sr}_3\text{Ru}_2\text{O}_7$. *Phys. Rev. Lett.*, 101:026407, Jul 2008.
- [116] Z. Q. Mao, M. Zhou, J. Hooper, V. Golub, and C. J. O'Connor. Phase separation in the itinerant metamagnetic transition of $\text{Sr}_4\text{Ru}_3\text{O}_{10}$. *Phys. Rev. Lett.*, 96:077205, Feb 2006.
- [117] V. Granata, L. Capogna, F. Forte, M.-B. Lepetit, R. Fittipaldi, A. Stunault, M. Cuoco, and A. Vecchione. Spin-orbital nature of the high-field magnetic state in the $\text{Sr}_4\text{Ru}_3\text{O}_{10}$. *Phys. Rev. B*, 93:115128, Mar 2016.
- [118] Y. Luo, C. Cao, B. Si, Y. Li, J. Bao, H. Guo, X. Yang, C. Shen, C. Feng, J. Dai, G. Cao, and Z. Xu. Li_2RhO_3 : A spin-glassy relativistic Mott insulator. *Phys. Rev. B*, 87:161121, Apr 2013.
- [119] I. I. Mazin, S. Manni, K. Foyevtsova, Harald O. Jeschke, P. Gegenwart, and R. Valentí. Origin of the insulating state in honeycomb iridates and rhodates. *Phys. Rev. B*, 88:035115, Jul 2013.
- [120] F. Baumberger, N. J. C. Ingle, W. Meevasana, K. M. Shen, D. H. Lu, R. S. Perry, A. P. Mackenzie, Z. Hussain, D. J. Singh, and Z.-X. Shen. Fermi surface and quasiparticle excitations of Sr_2RhO_4 . *Phys. Rev. Lett.*, 96:246402, Jun 2006.

- [121] R. S. Perry, F. Baumberger, L. Balicas, N. Kikugawa, N. J. C. Ingle, A. Rost, J. F. Mercure, Y. Maeno, Z. X. Shen, and A. P. Mackenzie. Sr_2RhO_4 : A new, clean correlated electron metal. *New Journal of Physics*, 8(9):175, 2006.
- [122] S. Calder, L. Li, S. Okamoto, Y. Choi, R. Mukherjee, D. Haskel, and D. Mandrus. Spin-orbit driven magnetic insulating state with $J_{\text{eff}} = \frac{1}{2}$ character in a $4d$ oxide. *Phys. Rev. B*, 92:180413, Nov 2015.
- [123] G. Cao, S. Parkin, and P. Schlottmann. Magnetic anisotropy and geometrical frustration in the ising spin-chain system $\text{Sr}_5\text{Rh}_4\text{O}_{12}$. *Solid State Communications*, 141(7):369 – 373, 2007.
- [124] M.-C. Jung and K.-W. Lee. Electronic structures, magnetism, and phonon spectra in the metallic cubic perovskite BaOsO_3 . *Phys. Rev. B*, 90:045120, Jul 2014.
- [125] Y. Shi, Y. Guo, Y. Shirako, W. Yi, X. Wang, A. A. Belik, Y. Matsushita, H. L. Feng, Y. Tsujimoto, M. Arai, N. Wang, M. Akaogi, and K. Yamaura. High-pressure synthesis of $5d$ cubic perovskite BaOsO_3 at 17 GPa: Ferromagnetic evolution over $3d$ to $5d$ series. *Journal of the American Chemical Society*, 135(44):16507–16516, 2013.
- [126] D. Mandrus, J. R. Thompson, R. Gaal, L. Forro, J. C. Bryan, B. C. Chakoumakos, L. M. Woods, B. C. Sales, R. S. Fishman, and V. Keppens. Continuous metal-insulator transition in the pyrochlore $\text{Cd}_2\text{Os}_2\text{O}_7$. *Phys. Rev. B*, 63:195104, Apr 2001.
- [127] W. J. Padilla, D. Mandrus, and D. N. Basov. Searching for the Slater transition in the pyrochlore $\text{Cd}_2\text{Os}_2\text{O}_7$ with infrared spectroscopy. *Phys. Rev. B*, 66:035120, Jul 2002.
- [128] N. A. Bogdanov, R. Maurice, I. Rousochatzakis, J. van den Brink, and L. Hozoi. Magnetic state of pyrochlore $\text{Cd}_2\text{Os}_2\text{O}_7$ emerging from strong competition of ligand distortions and longer-range crystalline anisotropy. *Phys. Rev. Lett.*, 110:127206, Mar 2013.
- [129] C. H. Sohn, H. Jeong, H. Jin, S. Kim, L. J. Sandilands, H. J. Park, K. W. Kim, S. J. Moon, D.-Y. Cho, J. Yamaura, Z. Hiroi, and T. W. Noh. Optical spectroscopic studies of the metal-insulator transition driven by all-in/all-out magnetic ordering in $5d$ pyrochlore $\text{Cd}_2\text{Os}_2\text{O}_7$. *Phys. Rev. Lett.*, 115:266402, Dec 2015.
- [130] K.-W. Lee and W. E. Pickett. Orbital-quenching-induced magnetism in $\text{Ba}_2\text{NaOsO}_6$. *EPL (Europhysics Letters)*, 80(3):37008, 2007.
- [131] A. J. Steele, P. J. Baker, T. Lancaster, F. L. Pratt, I. Franke, S. Ghannadzadeh, P. A. Goddard, W. Hayes, D. Prabhakaran, and S. J. Blundell. Low-moment magnetism in the double perovskites Ba_2MOsO_6 ($M=\text{Li,Na}$). *Phys. Rev. B*, 84:144416, Oct 2011.
- [132] S. Gangopadhyay and W. E. Pickett. Spin-orbit coupling, strong correlation, and insulator-metal transitions: The $j_{\text{eff}} = \frac{3}{2}$ ferromagnetic dirac-Mott insulator $\text{Ba}_2\text{NaOsO}_6$. *Phys. Rev. B*, 91:045133, Jan 2015.
- [133] C. M. Thompson, J. P. Carlo, R. Flacau, T. Aharen, I. A. Leahy, J. R. Pollicemi, T. J. S. Munsie, T. Medina, G. M. Luke, J. Munevar, S. Cheung, T. Goko, Y. J. Uemura, and

- J. E. Greedan. Long-range magnetic order in the $5d^2$ double perovskite $\text{Ba}_2\text{CaOsO}_6$: Comparison with spin-disordered Ba_2YReO_6 . *Journal of Physics: Condensed Matter*, 26(30):306003, 2014.
- [134] S. Gangopadhyay and W. E. Pickett. Interplay between spin-orbit coupling and strong correlation effects: Comparison of the three osmate double perovskites Ba_2AOsO_6 ($\text{A}=\text{Na}$, Ca , Y). *Phys. Rev. B*, 93:155126, Apr 2016.
- [135] E. Kermarrec, C. A. Marjerrison, C. M. Thompson, D. D. Maharaj, K. Levin, S. Kroeker, G. E. Granroth, R. Flacau, Z. Yamani, J. E. Greedan, and B. D. Gaulin. Frustrated fcc antiferromagnet Ba_2YOsO_6 : Structural characterization, magnetic properties, and neutron scattering studies. *Phys. Rev. B*, 91:075133, Feb 2015.
- [136] Q. Huang, J. L. Soubeyroux, O. Chmaissem, I. Natali Sora, A. Santoro, R. J. Cava, J. J. Krajewski, and W. F. Peck. Neutron Powder Diffraction Study of the Crystal Structures of Sr_2RuO_4 and Sr_2IrO_4 at Room Temperature and at 10K. *Journal of Solid State Chemistry*, 112(2):355, 1994.
- [137] S. J. Moon, Hosub Jin, W. S. Choi, J. S. Lee, S. S. A. Seo, J. Yu, G. Cao, T. W. Noh, and Y. S. Lee. Temperature dependence of the electronic structure of the $J_{\text{eff}} = \frac{1}{2}$ Mott insulator Sr_2IrO_4 studied by optical spectroscopy. *Phys. Rev. B*, 80:195110, Nov 2009.
- [138] G. Cao, J. Bolivar, S. McCall, J. E. Crow, and R. P. Guertin. Weak ferromagnetism, metal-to-nonmetal transition, and negative differential resistivity in single-crystal Sr_2IrO_4 . *Phys. Rev. B*, 57(18):R11039, May 1998.
- [139] H. Jin, H. Jeong, T. Ozaki, and J. Yu. Anisotropic exchange interactions of spin-orbit-integrated states in Sr_2IrO_4 . *Phys. Rev. B*, 80(7):075112, Aug. 2009.
- [140] H. Watanabe, T. Shirakawa, and S. Yunoki. Microscopic Study of a Spin-Orbit-Induced Mott Insulator in Ir Oxides. *Phys. Rev. Lett.*, 105(21):216410, Nov 2010.
- [141] S. Fujiyama, H. Ohsumi, K. Ohashi, D. Hirai, B. J. Kim, T. Arima, M. Takata, and H. Takagi. Spin and orbital contributions to magnetically ordered moments in $5d$ layered perovskite Sr_2IrO_4 . *Phys. Rev. Lett.*, 112:016405, Jan 2014.
- [142] P. Liu, S. Khmelevskiy, B. Kim, M. Marsman, D. Li, X.-Q. Chen, D. D. Sarma, G. Kresse, and C. Franchini. Anisotropic magnetic couplings and structure-driven canted to collinear transitions in Sr_2IrO_4 by magnetically constrained noncollinear DFT. *Phys. Rev. B*, 92:054428, Aug 2015.
- [143] J. Dai, E. Calleja, G. Cao, and K. McElroy. Local density of states study of a spin-orbit-coupling induced Mott insulator Sr_2IrO_4 . *Phys. Rev. B*, 90:041102, Jul 2014.
- [144] V. Brouet, J. Mansart, L. Perfetti, C. Piovera, I. Vobornik, P. Le Fèvre, F. Bertran, S. C. Riggs, M. C. Shapiro, P. Giraldo-Gallo, and I. R. Fisher. Transfer of spectral weight across the gap of Sr_2IrO_4 induced by La doping. *Phys. Rev. B*, 92:081117, Aug 2015.

- [145] C. Piovera, V. Brouet, E. Papalazarou, M. Caputo, M. Marsi, A. Taleb-Ibrahimi, B. J. Kim, and L. Perfetti. Time-resolved photoemission of Sr_2IrO_4 . *Phys. Rev. B*, 93:241114, Jun 2016.
- [146] D. Hsieh, F. Mahmood, D. H. Torchinsky, G. Cao, and N. Gedik. Observation of a metal-to-insulator transition with both Mott-Hubbard and Slater characteristics in Sr_2IrO_4 from time-resolved photocarrier dynamics. *Phys. Rev. B*, 86:035128, Jul 2012.
- [147] Turan Birol and Kristjan Haule. $J_{\text{eff}} = 1/2$ Mott-insulating state in Rh and Ir fluorides. *Phys. Rev. Lett.*, 114:096403, Mar 2015.
- [148] A. de la Torre, S. McKeown Walker, F. Y. Bruno, S. Ricc , Z. Wang, I. Gutierrez Lezama, G. Scheerer, G. Giriat, D. Jaccard, C. Berthod, T. K. Kim, M. Hoesch, E. C. Hunter, R. S. Perry, A. Tamai, and F. Baumberger. Collapse of the Mott gap and emergence of a nodal liquid in lightly doped Sr_2IrO_4 . *Phys. Rev. Lett.*, 115:176402, Oct 2015.
- [149] Tom Hogan, Z. Yamani, D. Walkup, Xiang Chen, Rebecca Dally, Thomas Z. Ward, M. P. M. Dean, John Hill, Z. Islam, Vidya Madhavan, and Stephen D. Wilson. First-order melting of a weak spin-orbit Mott insulator into a correlated metal. *Phys. Rev. Lett.*, 114:257203, Jun 2015.
- [150] J.-G. Cheng, J.-S. Zhou, J. B. Goodenough, Y. Sui, Y. Ren, and M. R. Suchomel. High-pressure synthesis and physical properties of perovskite and post-perovskite $\text{Ca}_{1-x}\text{Sr}_x\text{IrO}_3$. *Phys. Rev. B*, 83:064401, Feb 2011.
- [151] J. Gunasekera, L. Harriger, A. Dahal, T. Heitmann, G. Vignale, and D. K. Singh. Magnetic fluctuations driven insulator-to-metal transition in $\text{CaIr}_{1-x}\text{Ru}_x\text{O}_3$. *Scientific Reports*, 5:18047, Sep 2015.
- [152] T. F. Qi, O. B. Korneta, L. Li, K. Butrouna, V. S. Cao, Xiangang Wan, P. Schlottmann, R. K. Kaul, and G. Cao. Spin-orbit tuned metal-insulator transitions in single-crystal $\text{Sr}_2\text{Ir}_{1-x}\text{Rh}_x\text{O}_4$ ($0 \leq x \leq 1$). *Phys. Rev. B*, 86:125105, Sep 2012.
- [153] S. Chikara, D. Haskel, J.-H. Sim, H.-S. Kim, C.-C. Chen, G. Fabbri, L. S. I. Veiga, N. M. Souza-Neto, J. Terzic, K. Butrouna, G. Cao, M. J. Han, and M. van Veenendaal. $\text{Sr}_2\text{Ir}_{1-x}\text{Rh}_x\text{O}_4$ ($x < 0.5$): An inhomogeneous $J_{\text{eff}} = \frac{1}{2}$ Hubbard system. *Phys. Rev. B*, 92:081114, Aug 2015.
- [154] S. Calder, J. W. Kim, G.-X. Cao, C. Cantoni, A. F. May, H. B. Cao, A. A. Aczel, M. Matsuda, Y. Choi, D. Haskel, B. C. Sales, D. Mandrus, M. D. Lumsden, and A. D. Christianson. Evolution of competing magnetic order in the $J_{\text{eff}} = 1/2$ insulating state of $\text{Sr}_2\text{Ir}_{1-x}\text{Ru}_x\text{O}_4$. *Phys. Rev. B*, 92:165128, Oct 2015.
- [155] Brendan F. Phelan, Jason Krizan, Weiwei Xie, Quinn Gibson, and R. J. Cava. New material for probing spin-orbit coupling in iridates. *Phys. Rev. B*, 91:155117, Apr 2015.
- [156] G.-Q. Liu. Spin-orbit coupling induced Mott transition in $\text{Ca}_{2-x}\text{Sr}_x\text{RuO}_4$ ($0 \leq x \leq 0.2$). *Phys. Rev. B*, 84:235136, Dec 2011.

- [157] W. J. Kim, S. Y. Kim, C. H. Kim, C. H. Sohn, O. B. Korneta, S. C. Chae, and T. W. Noh. Spin-orbit coupling induced band structure change and orbital character of epitaxial IrO₂ films. *Phys. Rev. B*, 93:045104, Jan 2016.
- [158] S. K. Panda, S. Bhowal, A. Delin, O. Eriksson, and I. Dasgupta. Effect of spin orbit coupling and Hubbard U on the electronic structure of IrO₂. *Phys. Rev. B*, 89:155102, Apr 2014.
- [159] J. M. Kahk, C. G. Poll, F. E. Oropeza, J. M. Ablett, D. Céolin, J-P. Rueff, S. Agrestini, Y. Utsumi, K. D. Tsuei, Y. F. Liao, F. Borgatti, G. Panaccione, A. Regoutz, R. G. Egdel, B. J. Morgan, D. O. Scanlon, and D. J. Payne. Understanding the electronic structure of IrO₂ using hard-X-ray photoelectron spectroscopy and density-functional theory. *Phys. Rev. Lett.*, 112:117601, Mar 2014.
- [160] B. N. Figgis and J. Lewis. *The Magnetic Properties of Transition Metal Complexes*, pages 37–239. John Wiley & Sons, Inc., 2007.
- [161] P. Schwerdtfeger. *Relativistic Electronic Structure Theory, Part 2: Applications*. Elsevier, 2004.
- [162] J. Friedel. *The Physics of Metals, Electrons*. in Ziman, J.M. (Ed), Cambridge University Press, Cambridge, 1969.
- [163] S. Calder, G.-X. Cao, M. D. Lumsden, J. W. Kim, Z. Gai, B. C. Sales, D. Mandrus, and A. D. Christianson. Magnetic structural change of Sr₂IrO₄ upon Mn doping. *Phys. Rev. B*, 86:220403, Dec 2012.
- [164] A. I. Lichtenstein and M. I. Katsnelson. Ab initio calculations of quasiparticle band structure in correlated systems: LDA++ approach. *Phys. Rev. B*, 57(12):6884, Mar. 1998.
- [165] V. I. Anisimov, A. I. Poteryaev, M. A. Korotin, A. O. Anokhin, and G. Kotliar. First-principles calculations of the electronic structure and spectra of strongly correlated systems: Dynamical mean-field theory. *Journal of Physics: Condensed Matter*, 9(35):7359, Sep. 1997.
- [166] S. Biermann. Electronic structure of transition metal compounds: DFT-DMFT approach. In *Encyclopedia of Materials: Science and Technology (Second Edition)*, pages 1 – 9. Elsevier, Oxford, second edition edition, 2006.
- [167] S. Biermann. Dynamical screening effects in correlated electron materialsa progress report on combined many-body perturbation and dynamical mean field theory: GW+DMFT. *Journal of Physics: Condensed Matter*, 26(17):173202, 2014.
- [168] S. Biermann, A. Dallmeyer, C. Carbone, W. Eberhardt, C. Pampuch, O. Rader, M. I. Katsnelson, and A. I. Lichtenstein. Observation of Hubbard bands in γ -manganese. *JETP Letters*, 80:612, 2004.
- [169] A. I. Lichtenstein, M. I. Katsnelson, and G. Kotliar. Finite-temperature magnetism of transition metals: An *ab initio* dynamical mean-field theory. *Phys. Rev. Lett.*, 87:067205, Jul 2001.

- [170] J. Braun, J. Minár, H. Ebert, M. I. Katsnelson, and A. I. Lichtenstein. Spectral function of ferromagnetic $3d$ metals: A self-consistent LSDA+DMFT approach combined with the one-step model of photoemission. *Phys. Rev. Lett.*, 97:227601, Dec 2006.
- [171] J. Sánchez-Barriga, J. Minár, J. Braun, A. Varykhalov, V. Boni, I. Di Marco, O. Rader, V. Bellini, F. Manghi, H. Ebert, M. I. Katsnelson, A. I. Lichtenstein, O. Eriksson, W. Eberhardt, H. A. Dürr, and J. Fink. Quantitative determination of spin-dependent quasiparticle lifetimes and electronic correlations in hcp cobalt. *Phys. Rev. B*, 82:104414, Sep 2010.
- [172] S. Biermann, A. Poteryaev, A. I. Lichtenstein, and A. Georges. Dynamical singlets and correlation-assisted Peierls transition in VO_2 . *Phys. Rev. Lett.*, 94:026404, Jan 2005.
- [173] J. M. Tomczak and S. Biermann. Effective band structure of correlated materials: The case of VO_2 . *Journal of Physics: Condensed Matter*, 19(36):365206, 2007.
- [174] J. M. Tomczak and S. Biermann. Materials design using correlated oxides: Optical properties of vanadium dioxide. *EPL (Europhysics Letters)*, 86(3):37004, 2009.
- [175] J. M. Tomczak and S. Biermann. Optical properties of correlated materials: Generalized Peierls approach and its application to VO_2 . *Phys. Rev. B*, 80:085117, Aug 2009.
- [176] J. M. Tomczak and S. Biermann. Multi-orbital effects in optical properties of vanadium sesquioxide. *Journal of Physics: Condensed Matter*, 21(6):064209, 2009.
- [177] P. Thunström, I. Di Marco, and O. Eriksson. Electronic entanglement in late transition metal oxides. *Phys. Rev. Lett.*, 109:186401, Oct 2012.
- [178] F. Lechermann, S. Biermann, and A. Georges. Competing itinerant and localized states in strongly correlated BaVS_3 . *Phys. Rev. B*, 76:085101, 2007.
- [179] F. Lechermann, S. Biermann, and A. Georges. Importance of interorbital charge transfers for the metal-to-insulator transition of BaVS_3 . *Phys. Rev. Lett.*, 94:166402, Apr 2005.
- [180] M. Aichhorn, L. Pourovskii, V. Vildosola, M. Ferrero, O. Parcollet, T. Miyake, A. Georges, and S. Biermann. Dynamical mean-field theory within an augmented plane-wave framework: Assessing electronic correlations in the iron pnictide LaFeAsO . *Phys. Rev. B*, 80(8):085101, Aug. 2009.
- [181] T. Miyake, K. Nakamura, R. Arita, and M. Imada. Comparison of ab initio low-energy models for LaFePO , LaFeAsO , BaFe_2As_2 , LiFeAs , FeSe , and FeTe : Electron correlation and covalency. *Journal of the Physical Society of Japan*, 79(4):044705, 2010.
- [182] B. Amadon, S. Biermann, A. Georges, and F. Aryasetiawan. The α - γ transition of cerium is entropy driven. *Phys. Rev. Lett.*, 96:066402, Feb 2006.
- [183] M. B. Zöfl, I. A. Nekrasov, T. Pruschke, V. I. Anisimov, and J. Keller. Spectral and Magnetic Properties of α - and γ -Ce from Dynamical Mean-Field Theory and Local Density Approximation. *Physical Review Letters*, 87(26):A266403+, December 2001.
- [184] J. Bieder and B. Amadon. Thermodynamics of the α - γ transition in cerium from first principles. *Phys. Rev. B*, 89:195132, May 2014.

- [185] L. V. Pourovskii, B. Amadon, S. Biermann, and A. Georges. Self-consistency over the charge density in dynamical mean-field theory: A linear muffin-tin implementation and some physical implications. *Phys. Rev. B*, 76:235101, Dec 2007.
- [186] L. Pourovskii, V. Vildosola, S. Biermann, and A. Georges. Local moment vs . Kondo behavior of the 4f-electrons in rare-earth iron oxypnictides. *EPL (Europhysics Letters)*, 84(3):37006, 2008.
- [187] T. Miyake, L. Pourovskii, V. Vildosola, S. Biermann, and A. Georges. d- and f-orbital correlations in the REFeAsO compounds. *Journal of the Physical Society of Japan*, 77(Suppl.C):99–102, 2008.
- [188] J. M. Tomczak, L. V. Pourovskii, L. Vaugier, A. Georges, and S. Biermann. Rare-earth vs. heavy metal pigments and their colors from first principles. *Proceedings of the National Academy of Sciences*, 110(3):904–907, 2013.
- [189] K. Haule, C.-H. Yee, and K. Kim. Dynamical mean-field theory within the full-potential methods: Electronic structure of CeIrIn₅, CeCoIn₅, and CeRhIn₅. *Phys. Rev. B*, 81(19):195107, May 2010.
- [190] L. V. Pourovskii, P. Hansmann, M. Ferrero, and A. Georges. Theoretical prediction and spectroscopic fingerprints of an orbital transition in CeCu₂Si₂. *Phys. Rev. Lett.*, 112:106407, Mar 2014.
- [191] S. Y. Savrasov, G. Kotliar, and E. Abrahams. Correlated electrons in δ -plutonium within a dynamical mean-field picture. *Nature*, 410(6830):793, 2001.
- [192] S. Y. Savrasov, K. Haule, and G. Kotliar. Many-body electronic structure of americium metal. *Phys. Rev. Lett.*, 96:036404, Jan 2006.
- [193] J. Kolorenc, A. B. Shick, and A. I. Lichtenstein. Electronic structure and core-level spectra of light actinide dioxides in the dynamical mean-field theory. *Phys. Rev. B*, 92:085125, Aug 2015.
- [194] L. V. Pourovskii, M. I. Katsnelson, and A. I. Lichtenstein. Correlation effects in electronic structure of actinide monochalcogenides. *Phys. Rev. B*, 72:115106, Sep 2005.
- [195] J. Ferber, K. Foyevtsova, H. O. Jeschke, and R. Valentí. Unveiling the microscopic nature of correlated organic conductors: The case of κ -ET₂Cu[N(CN)₂]Br_xCl_{1-x}. *Phys. Rev. B*, 89:205106, May 2014.
- [196] J. M. Tomczak, K. Haule, T. Miyake, A. Georges, and G. Kotliar. Thermopower of correlated semiconductors: Application to FeAs₂ and FeSb₂. *Phys. Rev. B*, 82:085104, Aug 2010.
- [197] P. Sun, W. Xu, J. M. Tomczak, G. Kotliar, M. Sondergaard, B. B. Iversen, and F. Steglich. Highly dispersive electron relaxation and colossal thermoelectricity in the correlated semiconductor FeSb₂. *Phys. Rev. B*, 88:245203, Dec 2013.

- [198] Motoaki Hirayama, Takashi Miyake, and Masatoshi Imada. Ab initio low-energy model of transition-metal-oxide heterostructure $\text{LaAlO}_3/\text{SrTiO}_3$. *Journal of the Physical Society of Japan*, 81(8):084708, 2012.
- [199] P. Hansmann, T. Ayral, L. Vaugier, P. Werner, and S. Biermann. Long-range Coulomb interactions in surface systems: A first-principles description within self-consistently combined GW and dynamical mean-field theory. *Phys. Rev. Lett.*, 110:166401, Apr 2013.
- [200] P. Hansmann, T. Ayral, A. Tejada, and S. Biermann. Uncertainty principle for experimental measurements: Fast versus slow probes. *Scientific Reports*, 6:19728, 2016.
- [201] S. Biermann, F. Aryasetiawan, and A. Georges. First-principles approach to the electronic structure of strongly correlated systems: Combining the GW approximation and dynamical mean-field theory. *Phys. Rev. Lett.*, 90(8):086402, Feb 2003.
- [202] T. Ayral, P. Werner, and S. Biermann. Spectral properties of correlated materials: Local vertex and nonlocal two-particle correlations from combined GW and dynamical mean field theory. *Phys. Rev. Lett.*, 109:226401, Nov 2012.
- [203] T. Ayral, S. Biermann, and P. Werner. Screening and nonlocal correlations in the extended Hubbard model from self-consistent combined GW and dynamical mean field theory. *Phys. Rev. B*, 87:125149, Mar 2013.
- [204] A. van Roekeghem and S. Biermann. Screened exchange dynamical mean-field theory and its relation to density functional theory: SrVO_3 and SrTiO_3 . *EPL (Europhysics Letters)*, 108(5):57003, 2014.
- [205] S. Biermann. Dynamical screening effects in correlated electron materials a progress report on combined many-body perturbation and dynamical mean field theory: GW + DMFT. *Journal of Physics: Condensed Matter*, 26(17):173202, 2014.
- [206] L. Vaugier, H. Jiang, and S. Biermann. Hubbard U and Hund exchange J in transition metal oxides: Screening versus localization trends from constrained random phase approximation. *Phys. Rev. B*, 86:165105, Oct 2012.
- [207] V. I. Anisimov, D. E. Kondakov, A. V. Kozhevnikov, I. A. Nekrasov, Z. V. Pchelkina, J. W. Allen, S.-K. Mo, H.-D. Kim, P. Metcalf, S. Suga, A. Sekiyama, G. Keller, I. Leonov, X. Ren, and D. Vollhardt. Full orbital calculation scheme for materials with strongly correlated electrons. *Phys. Rev. B*, 71:125119, Mar 2005.
- [208] F. Lechermann, A. Georges, A. Poteryaev, S. Biermann, M. Posternak, A. Yamasaki, and O. K. Andersen. Dynamical mean-field theory using Wannier functions: A flexible route to electronic structure calculations of strongly correlated materials. *Phys. Rev. B*, 74:125120, Sep 2006.
- [209] M. Aichhorn, L. Pourovskii, P. Seth, V. Vildosola, M. Zingl, O. E. Peil, X. Deng, J. Mravlje, G. J. Krabberger, C. Martins, M. Ferrero, and O. Parcollet. TRIQS/DFTTools: A TRIQS application for ab initio calculations of correlated materials. *Computer Physics Communications*, 204:200 – 208, 2016.

- [210] P. Blaha, K. Schwarz, G. Madsen, D. Kvasnicka, and J. Luitz. *Wien2k, An Augmented Plane Wave+Local Orbitals Program for Calculating Crystal Properties*. Karlheinz Schwarz, Tech. Universität Wien, Austria, 2001.
- [211] C. Martins. *Interplay of Spin-Orbit Coupling and Electronic Coulomb Interactions in Strontium Iridate Sr_2IrO_4* . PhD thesis, Ecole Polytechnique, 2010.
- [212] A. V. Shubnikov. *Symmetry and Antisymmetry of Finite Figures*. USSR Academy of Sciences, Moscow, 1951.
- [213] F. Aryasetiawan, M. Imada, A. Georges, G. Kotliar, S. Biermann, and A. I. Lichtenstein. Frequency-dependent local interactions and low-energy effective models from electronic structure calculations. *Phys. Rev. B*, 70:195104, Nov 2004.
- [214] Takashi Miyake and F. Aryasetiawan. Screened Coulomb interaction in the maximally localized Wannier basis. *Phys. Rev. B*, 77:085122, Feb 2008.
- [215] F. Aryasetiawan, K. Karlsson, O. Jepsen, and U. Schönberger. Calculations of Hubbard U from first-principles. *Phys. Rev. B*, 74:125106, Sep 2006.
- [216] J. M. Tomczak, T. Miyake, and F. Aryasetiawan. Realistic many-body models for manganese monoxide under pressure. *Phys. Rev. B*, 81:115116, Mar 2010.
- [217] R. Sakuma and F. Aryasetiawan. First-principles calculations of dynamical screened interactions for the transition metal oxides mo ($m=mn, fe, co, ni$). *Phys. Rev. B*, 87:165118, Apr 2013.
- [218] T. Miyake, L. Pourovskii, V. Vildosola, S. Biermann, and A. Georges. d- and f-orbital correlations in the REFeAsO compounds. *Journal of the Physical Society of Japan*, 77(Suppl.C):99–102, 2008.
- [219] K. Nakamura, R. Arita, and M. Imada. Ab initio derivation of low-energy model for iron-based superconductors LaFeAsO and LaFePO. *Journal of the Physical Society of Japan*, 77(9):093711, 2008.
- [220] M. Imada and T. Miyake. Electronic structure calculation by first principles for strongly correlated electron systems. *Journal of the Physical Society of Japan*, 79(11):112001, 2010.
- [221] F. Nilsson, R. Sakuma, and F. Aryasetiawan. *Ab initio* calculations of the Hubbard U for the early lanthanides using the constrained random-phase approximation. *Phys. Rev. B*, 88:125123, Sep 2013.
- [222] P. Hansmann, L. Vaugier, H. Jiang, and S. Biermann. What about U on surfaces? Extended Hubbard models for adatom systems from first principles. *Journal of Physics: Condensed Matter*, 25(9):094005, 2013.
- [223] I. V. Solovyev and M. Imada. Screening of coulomb interactions in transition metals. *Phys. Rev. B*, 71:045103, Jan 2005.
- [224] E. Şaşıoğlu, C. Friedrich, and S. Blügel. Effective Coulomb interaction in transition metals from constrained random-phase approximation. *Phys. Rev. B*, 83:121101, Mar 2011.

- [225] N. Marzari and D. Vanderbilt. Maximally localized generalized Wannier functions for composite energy bands. *Phys. Rev. B*, 56:12847–12865, Nov 1997.
- [226] P. Werner, A. Comanac, L. de’ Medici, M. Troyer, and A. J. Millis. Continuous-Time Solver for Quantum Impurity Models. *Phys. Rev. Lett.*, 97(7):076405, Aug. 2006.
- [227] K. S. D. Beach. Identifying the maximum entropy method as a special limit of stochastic analytic continuation. *arXiv:cond-mat/0403055 (unpublished)*, 2004.
- [228] M. K. Crawford, M. A. Subramanian, R. L. Harlow, J. A. Fernandez-Baca, Z. R. Wang, and D. C. Johnston. Structural and magnetic studies of Sr_2IrO_4 . *Phys. Rev. B*, 49(13):9198, Apr. 1994.
- [229] T. Vogt and D. J. Buttrey. Temperature dependent structural behavior of Sr_2RhO_4 . *Journal of Solid State Chemistry*, 123(1):186 – 189, 1996.
- [230] O. Chmaissem, J. D. Jorgensen, H. Shaked, S. Ikeda, and Y. Maeno. Thermal expansion and compressibility of Sr_2RuO_4 . *Phys. Rev. B*, 57:5067–5070, Mar 1998.
- [231] S. Florens, A. Georges, G. Kotliar, and O. Parcollet. Mott transition at large orbital degeneracy: Dynamical mean-field theory. *Phys. Rev. B*, 66:205102, Nov 2002.